The Chicxulub impact and its environmental consequences

Joanna V. Morgan[1]✉*, Timothy J. Bralower*[2]*, Julia Brugger*[3,4] *and Kai Wünnemann*[5,6]

Abstract | The extinction of the dinosaurs and around three-quarters of all living species was almost certainly caused by a large asteroid impact 66 million years ago. Seismic data acquired across the impact site in Mexico have provided spectacular images of the approximately 200-kilometre-wide Chicxulub impact structure. In this Review, we show how studying the impact site at Chicxulub has advanced our understanding of formation of large craters and the environmental and palaeontological consequences of this impact. The Chicxulub crater's asymmetric shape and size suggest an oblique impact and an impact energy of about 10^{23} joules, information that is important for quantifying the climatic effects of the impact. Several thousand gigatonnes of asteroidal and target material were ejected at velocities exceeding 5 kilometres per second, forming a fast-moving cloud that transported dust, soot and sulfate aerosols around the Earth within hours. These impact ejecta and soot from global wildfires blocked sunlight and caused global cooling, thus explaining the severity and abruptness of the mass extinction. However, it remains uncertain whether this impact winter lasted for many months or for more than a decade. Further combined palaeontological and proxy studies of expanded Cretaceous–Palaeogene transitions should further constrain the climatic response and the precise cause and selectivity of the extinction.

[1]*Department of Earth Science and Engineering, Imperial College London, London, UK.*

[2]*Department of Geosciences, Pennsylvania State University, University Park, PA, USA.*

[3]*Senckenberg Biodiversity and Climate Research Centre, Frankfurt am Main, Germany.*

[4]*Earth System Analysis, Potsdam Institute for Climate Impact Research, Member of the Leibniz Association, Potsdam, Germany.*

[5]*Museum für Naturkunde, Leibniz Institute for Evolution and Biodiversity Science, Berlin, Germany.*

[6]*Institute of Geological Sciences, Planetary Sciences and Remote Sensing, Freie Universität Berlin, Berlin, Germany.*

✉*e-mail: j.v.morgan@imperial.ac.uk*

https://doi.org/10.1038/s43017-022-00283-y

The extinction of the dinosaurs and three-quarters of all species on the Earth[1–3] coincides with a thin layer of clay separating rocks from the Mesozoic and Cenozoic eras in the global geological record. In 1980, evidence that this clay layer had an extra-terrestrial signature led to the theory that the impact of a large meteorite was responsible for the K-Pg boundary mass extinction[4,5]. Although volcanic eruptions at the Deccan Traps in India and elsewhere might have initiated climatic changes around the same time[6,7], outgassing of CO_2 from the Deccan had concluded prior to the K–Pg impact before beginning again in the earliest Palaeocene[2,8]. The abruptness and severity of the marine extinction at the K–Pg boundary points to the impact being the principal cause[2,9–11].

On other planetary bodies, crater morphology changes clearly with increasing crater size, in a way that is dependent on gravity and near-surface rock properties[12]. Chicxulub is one of the largest types of crater, possessing a topographic ring of hills within the impact basin known as a peak ring[13,14]. As the most pristine large impact structure on the Earth, Chicxulub is critical for furthering our understanding of large cratering processes. Burial of the crater by several hundred metres of sedimentary rocks, and its location half offshore meant that it was readily accessible to high-resolution imaging with marine seismic surveys[14,15]. Its imaged structure was used to ground-truth a model of peak-ring formation[16,17], and this model was confirmed by IODP-ICDP (International Ocean Discovery Program, International Continental Scientific Drilling Program) scientific drilling into the peak ring in 2016 (REF.[18]) (Expedition 364). In large impacts, a bowl-shaped transient crater is initially formed and then collapses to form a wider, flatter, final crater (FIG. 1, BOX 1). Downthrown Cretaceous sedimentary rocks, located with seismic data, were used to reconstruct the original transient crater, because this provides a measure of the impact energy[14]. Asymmetries in the Chicxulub impact structure indicate that the angle of impact was oblique, which, along with impact energy, is an important factor for estimating the mass of dust and climatic active gases released by the impact[19].

Chicxulub is linked to a world-wide layer of ejecta and a mass extinction, meaning that it is a natural laboratory in which to study what happened on the Earth following this catastrophic event. Indeed, results from the IODP-ICDP scientific drilling have addressed fundamental cratering processes[18,20] and recorded the recovery of life in the ocean above the impact site[21–24]. Also, between 2017 and 2021, simulations of ejecta–atmosphere interactions have shown how ejecta can

Key points

- The Chicxulub impact ended the Mesozoic era and was almost certainly the principal cause of the Cretaceous–Palaeogene (K–Pg) mass extinction.
- Seismic images of the approximately 200-km-wide Chicxulub impact structure reveal that it has the same morphology as the largest impact basins on other solid planetary bodies, such as the Lise Meitner and Klenova craters on Venus.
- Rocks from the impact site and asteroid were ejected within an impact plume and ejecta curtain. Ejection velocity is a function of shock pressure, with the most-shocked rocks leaving the impact site at $>11\,\mathrm{km\,s^{-1}}$ (escape velocity).
- The high-velocity ejecta interacted with the Earth's atmosphere to form a fast-moving cloud that carried dust, soot, sulfate aerosols and other ejecta around the Earth within 4–5 hours of impact.
- Ejecta within the cloud, along with soot from wildfires, caused the Earth to become dark and cold for about a decade, and induced longer-term (decadal to millennial) temperature changes and chemical changes in the ocean.
- This extended impact winter explains the abruptness and severity of the mass extinction, as well as its selective impact on different organisms.

travel all around the globe[25], and there have been further constraints on impact angle[19] and improvements in post-impact climate simulations[26–30], which have improved our understanding of the severity and timescale of climatic changes, and their effect on life.

In this Review, we first describe what happens when a large meteorite strikes a solid planetary body, and explain how the different crater types are formed. We then introduce Chicxulub, and show a model of the Chicxulub impact structure with a selection of seismic images that were used to construct it. We explain how images of the crater were used to constrain crater formation and the angle and energy of impact, and why this is important for estimating the mass, velocity and physical state of material ejected from the impact site. We discuss the current best model for how ejecta travels around the world to form the global K–Pg boundary layer. Finally, simulations of the impact's climatic effects are discussed alongside the potential causes of the extinction, and the recovery of life at the impact site and around the globe.

Impact cratering

When a large cosmic object strikes the surface of the Earth or any other planetary body it triggers a sequence of short- and long-term processes, and results in the formation of a crater[12] (FIG. 1 and BOX 1). Whereas crater structures are scars that remain visible on geological timescales, for example, the cratered landscapes on the Moon[31,32], other processes such as the atmospheric and climatic effects of impact are not easily extracted from the geological record. This section reviews the size-dependent transition in crater morphology (FIG. 1), which is used for size classification of the Chicxulub structure, including the generation of a plume and ejecta curtain (BOX 1 and FIG. 1a,b), and the mechanics of crater formation.

Crater morphology. Active tectonic and surface processes on the Earth mean that the remnants of cosmic bombardment have been erased to a large extent by subduction or erosion, or buried by sedimentary rocks. Such processes explain why fewer craters are known on the Earth than in the cratered landscapes of, for example, the Moon[31–33]. Determining the size and morphology of terrestrial impact structures can be problematic when crater features are tectonically deformed, buried or eroded. Although the Chicxulub impact structure is well preserved because of its burial, this also means we must rely on geophysical methods to ascertain pre-burial topographic changes across the crater[14]. It is therefore important to compare Chicxulub's original morphology with the lunar crater record, which is considered a reference in terms of the typical surface expression of impact craters because of their relatively good long-term preservation[31].

The most striking observation from the lunar crater record is that crater morphology falls into two classes[12,32]: smaller, so-called simple craters (<15 km in diameter) that are bowl-shaped and larger, complex craters (>20 km in diameter) (FIG. 1) that have a flat interior floor and much smaller depth-to-diameter ratios. The rather smooth terrain inside them is thought to result from impact breccias and crystallized molten rocks (impact melt rocks) that cover the crater floor[31]. The Chicxulub crater falls into the second category.

Complex craters can be subdivided further into central peak and peak-ring craters, which are characterized by either a central cone-shaped structure or a ring of cones and peaks, respectively, that protrude out of the flat crater floor[12,31]. In both of these complex crater types, the flat basin is surrounded by an elevated crater rim formed by the outermost inward-facing head scarp of a terrace zone (FIG. 1c–f). The crater rim is considered to define the diameter of these two crater types[31,32]. Craters larger than approximately 300 km in diameter on the Moon exhibit multiple ring structures, formed from inward-facing tectonic scarps with smoother outward-facing slopes, of which the innermost ring might be a peak ring (FIG. 1g,h). Owing to the absence of a prominent crater rim, the size definition of multi-ring basins is often ambiguous.

The transition diameters, from central-peak crater to peak-ring crater and eventually to multi-ring basin (FIG. 1), are expected to be much smaller on the Earth and Venus because their gravity is approximately six times larger than the Moon's. On the Earth and Venus, impact

Fig. 1 | **The stages of complex impact crater formation.** ▶ Complex craters form when an initial bowl-shaped cavity (transient crater) collapses to form a final flat crater. **a** | In the excavation stage, rocks at the impact site are displaced to form a cavity with an uplifted rim, and ejected within an impact plume and ejecta curtain. **b** | In the modification stage, the cavity rim collapses downwards and inwards, whereas rocks in the central area initially collapse inwards and upwards and then downwards and outwards (see arrows). The size of the final crater increases with increasing impact energy. **c–h** | The morphology changes from a central-peak crater (part **c**), such as the the Tycho lunar crater (part **d**), to a peak-ring crater (part **e**), such as the lunar Schrödinger basin (part **f**), and finally a multi-ring basin (part **g**), such as the lunar Orientale basin (part **h**). Being relatively pristine, lunar craters play an important part in helping us to interpret the morphology of terrestrial craters, such as Chicxulub. Parts **d**, **f** and **h** credit: NASA/Goddard/Arizona State University/Lunar Reconnaissance Orbiter.

Cretaceous–Palaeogene (K–Pg) boundary
The boundary between the Mesozoic and Cenozoic eras, that marks the transition from the Cretaceous (K) period to the Palaeogene (Pg) period.

Peak ring
A circular feature within an impact basin composed of a ring of hills.

Impact structure
An impact crater that is covered, eroded or altered in some way.

Transient crater
The maximum size of the shock-induced bowl-shape cavity formed after collision. We note that the transient crater is rather a virtual construct, because the excavation flow ceased along the crater wall at different times. Collapse first occurs at the deepest point of the cavity and last near the pre-impact surface.

Ejecta curtain
Ejecta leaving the growing crater in the shape of a gradually expanding inverted cone.

Impact crater
The depression in the ground formed by a meteorite impact.

Impact melt rock
Solidified melt formed by high-pressure melting of rocks during an impact.

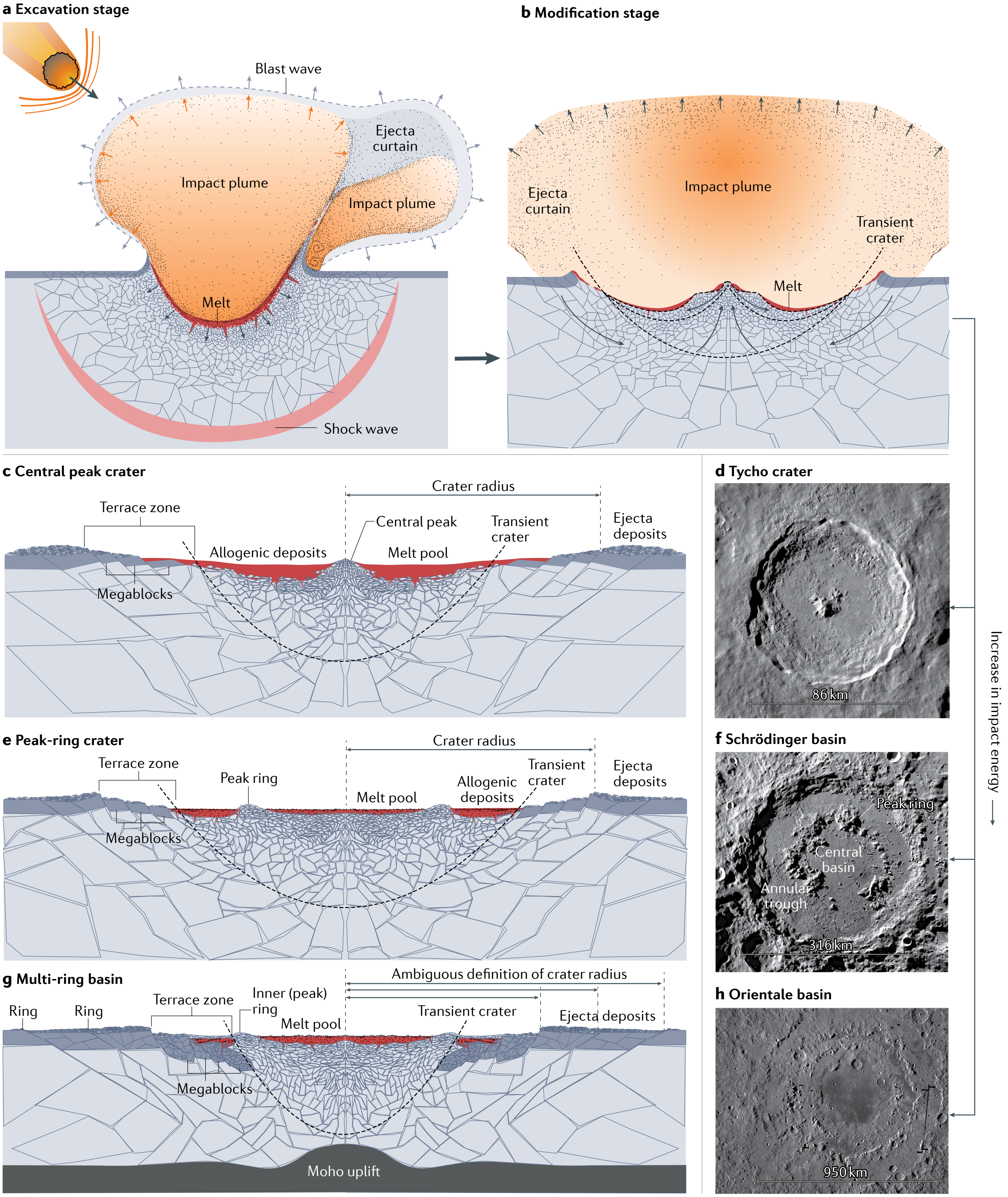

structures the size of Chicxulub (around 180–200 km in diameter[14,15,34]) are expected to correspond to the crater morphology of a multi-ring basin[35,36]. However, whether the morphology of the Chicxulub crater is indeed similar to that of typical multi-ring basins on the Moon, such as the Orientale crater (FIG. 1h), or whether it is comparable to that of a peak-ring crater such as the Schrödinger basin (FIG. 1f), is still a matter of debate[14,15,34]. Answering this question is essential to a better understanding of the formation of large craters.

Box 1 | The first ten minutes of a large impact

When an asteroid or comet penetrates into the target, it generates shock waves (FIG. 1a) with initial pressures of several hundreds of gigapascals[12]. The extreme thermodynamic conditions that occur during impact cause melting and vaporization of both the impactor and impacted target rocks[89], and the following impact processes.

Impact plume and ejecta curtain

An impact plume[172], composed of vaporized matter, melt shreds, lithic fragments and dust[63], rises from the growing cavity (FIG. 1a). The plume is bounded by a cone-shaped ejecta curtain[173] that is dominantly composed of target rocks and has more solid material than the plume[25]. The impact plume's initial temperature is several thousand kelvin[105] and the thermal radiation originating from it burns everything to a distance at which the plume drops below the horizon. The plume expands, decreases in density, cools and ascends hundreds of kilometres above the Earth. Lithic and condensed fragments, along with gaseous compounds from the impactor and vaporized rocks within the plume and upper part of the ejecta curtain, are ejected from the impact site with a velocity that is a function of shock pressure[64].

Blast wave

After thermal radiation from the impact plume, the second hazard is the blast wave (FIG. 1a), propagating through the atmosphere and knocking down anything in its path[174]. At the Earth's surface and close to the crater, the blast wave is closely followed by the arrival of material from the ejecta curtain.

Transient crater formation

Rocks at the impact site are set in motion by the shockwaves, and an initially bowl-shaped cavity (transient crater) is formed by the displacement and ejection of material. Transient craters are typically 10–20 times the diameter of the impactor[175–177] (FIG. 1a). If the transient crater is larger than 2–4 km across from rim to rim[175,176], the generated mass deficit triggers an upwards movement of target material to compensate for the loss (FIG. 1b). In the case of complex craters, the buoyant compensation of the mass deficit (the transient crater), can explain the uplift of deep-seated strata to the surface and the formation of central peaks[32].

Transient crater collapse and rock weakening

At the same time, the transient crater rim slumps downward and inward due to gravitational collapse (FIG. 1b) to form megablocks in a terrace zone (FIG. 1c,e,g). Such a gravity-driven upwelling flow at the centre has to overcome the strength and resistance of rocks against plastic deformation, which requires a fluid-like behaviour[176]. The fluid-like rheology inferred from impact craters[176] requires a rock-weakening mechanism that is temporary, as rocks have to regain some of their initial strength to eventually support the typical morphological characteristics such as central peaks and peak rings (FIG. 1c–e). The temporary weakening of rocks has been explained by a mechanism referred to as acoustic fluidization[73,176,178]. According to this theory, seismic vibrations in the wake of the shock wave cause small pressure fluctuations that are nevertheless sufficient to allow fragments and blocks to slip by each other, overcoming the frictional resistance imposed by the overburden pressure. As an alternative to acoustic fluidization, a dynamic fault-weakening model has also been proposed in which the transient crater collapses along a network of impact-generated faults[179]. In this model, high strain rates in the early stages of crater formation lead to a reduction in friction along these faults, allowing rocks to slip past one another[179,180].

Chicxulub

Knowing the size of the Chicxulub transient crater is central to constraining the energy of impact and its climatic consequences, whereas its structure and morphology are important for understanding the mechanics of large crater formation. Chicxulub can provide us with a better understanding of the formation of the size-dependent morphology of large impact structures on the Earth and other planetary bodies.

Discovering Chicxulub. In 1980 the K–Pg clay layer at sites in Europe was discovered to be rich in iridium[4,5]. Iridium is concentrated in extra-terrestrial materials and this led to the hypothesis that the Earth was hit by a large impactor and that this was the cause of the extinction of the dinosaurs. The iridium enrichment was found to be a global phenomenon, and the discovery that shocked minerals were also in the clay layer provided proof that it was formed by an impact[37,38]. Under a microscope, shocked minerals display a permanent deformation of the crystal lattice that can only be produced by a high-pressure shock wave passing through the rock; such minerals are only found within impactites and at nuclear test sites[39,40]. The only possible explanation for the presence of shocked quartz within the global K–Pg layer is that rocks containing quartz minerals at the impact site were shocked and ejected from the crater at high velocity and deposited around the globe.

Impactites
Rocks created or modified by one or more impacts of a meteorite.

The increase in size and number of shocked minerals at sites closer to Chicxulub[41], along with the increase in thickness and the high-energy mode of deposition of the K–Pg boundary layer, were used to track down the site of the impact[42]. Circular anomalies in gravity and magnetic data pinpointed its exact location within the Yucatán Peninsula, Mexico, and drill holes through the crater floor provided proof that Chicxulub was an impact structure of the right age[42,43]. The Yucatán carbonate platform was probably covered by a few hundred metres of water at the time of impact[15], and the crater is now buried by sedimentary rocks and located half onshore and half offshore (FIG. 2d).

Chicxulub structure, size and morphology. Following its discovery, a range of models of the Chicxulub impact structure were constructed using the available geophysical and drilling data. In these models, the crater was argued to be both 170 km and 300 km in diameter, and values in between, and to have the morphology of either a peak-ring crater or multi-ring basin[13,44–48] (FIG. 1e and g). These size extremes represent roughly an order-of-magnitude difference in impact energy. To resolve these differences and to map the Chicxulub impact structure in more detail, additional marine seismic data were acquired across the crater in 1996 and 2005 (REFS[14,15]) and the crater was sampled through ICDP and IODP scientific drilling at Yax 1 and M0077 (REF.[18]) (FIG. 2). The model of Chicxulub shown in FIG. 2a is consistent with all available geophysical and drilling data, as well as numerical simulations of crater formation[16–18].

Seismic reflection data reveal the structure of the offshore portion of the Chicxulub impact basin, including imaging of the Cretaceous sedimentary rocks (FIG. 2c), the top of the crater (FIG. 2b,c), the peak ring (FIG. 2b,c), and a terrace zone formed from Cretaceous megablocks[13–15,34,49,50] (FIG. 2a,c). The terrace zone is the remnant of the collapsed transient crater rim (FIG. 1b) and, for extra-terrestrial craters, only their outer edge can be seen (FIG. 1c,e). The observation that the terrace zone extended all the way to beneath the peak ring at Chicxulub was an important finding for ground-truthing models of crater formation[16]. Mohorovičić discontinuity (Moho) topography[49,51] and the top of the impact melt rocks (FIG. 2b,c) were also mapped with seismic reflection and refraction data[16,52,53]. Two other notable anomalies in seismic velocity models are the presence of rocks with high velocity close to the surface in the centre of the structure[16,54] (FIG. 2e), and relatively low-velocity rocks within

Suevitic impact breccia (or suevite)
A polymict impact breccia containing shocked and unshocked lithic and mineral clasts, and particles of impact melt rock.

the peak ring[16,52,53] (FIG. 2b). These velocity anomalies indicate that lower crustal rocks were uplifted >10 km in the centre of the crater (FIG. 2a), and that the impact melt rocks do not continue under the peak ring, as suggested in some early models of the Chicxulub impact structure[34,44].

The peak-ring rocks are covered by suevitic impact breccia[18,55–58], which can be identified as a low-velocity layer located between the top of the peak ring and a low-frequency reflector[52,59,60] (FIG. 2b). The breccias are interpreted as debris transported as a result of the ocean resurging back into the crater, as well as seiches (standing waves within the impact basin), and returning tsunami-like waves[55–58]. Suevitic impact breccia probably covers the whole crater floor, as indicated by the extension of the low-velocity layer into the annular trough and central basin[52] (FIG. 2b) and its occurrence in the onshore drill holes Y6, Yax-1, S-1 and C-1 (FIG. 2d).

In the marine seismic reflection data there are three consistent circular features (rings) with average radii of 40 km, 75 km and 95 km: a peak ring, the head scarp of the terrace zone, and an inward-facing asymmetric scarp[14,15,49] (FIG. 2a). On most reflection lines the head scarp of the terrace zone coincides with the edge

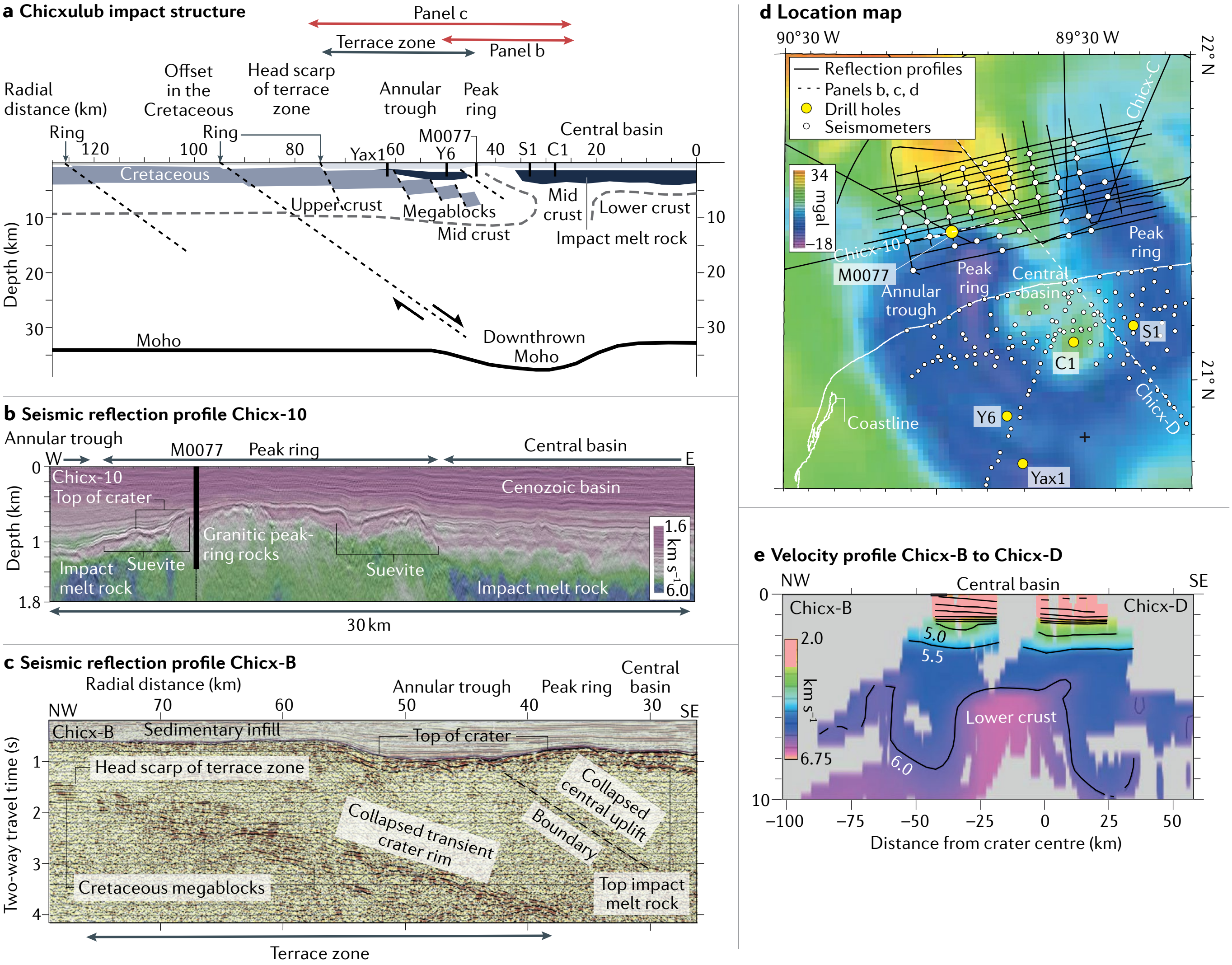

Fig. 2 | **The Chicxulub impact structure. a** | Model of the Chicxulub impact structure constructed using geophysical data, boreholes (Yax1, C1, S1, Y6, M0077) and numerical simulations[14,16–18,54,59,61]. Rings mark the location of asymmetric scarps. Inward-dipping reflectors connect one of these rings to a downthrown section of the Mohorovičić discontinuity (Moho). **b** | Seismic reflection profile Chicx-10 and velocity model across the Chicxulub peak ring. Drilling at site M0077 showed that the peak ring is formed from granitic basement rocks covered by impact melt rock and suevite[18,55,145,146]. The suevite has a high porosity and anomalously low seismic velocity, allowing it to be tracked across the peak ring, and into the annular trough and central basin[52,59,60]. **c** | Seismic reflection profile Chicx-B showing downthrown Cretaceous rocks that form a terrace zone below the annular trough and peak ring. Inward-dipping reflectors below the peak ring might correspond to the boundary between rocks from the collapsed central uplift and collapsed transient crater rim[16] (FIG. 1). Impact melt rocks were recovered in holes C1, S1 and Y6, at depths where a bright reflector (panel **c**) and an increase in seismic velocity (panel **b**) are observed. **d** | Location map showing experimental geometry and Bouguer gravity anomaly (colour scale in milligal, mGal). **e** | Velocity model along Chicx-B and -D. The high-velocity zone below the central basin, which is also associated with a Bouguer gravity high (panel **d**) and strong magnetic anomaly[44–46,171], is interpreted as uplifted lower crust[54,59,61]. The use of high-resolution geophysical data to place constraints on the structure of Chicxulub were key to ground-truthing models of large crater formation. Part **a** adapted with permission from REF.[58], Wiley. Parts **b** and **e** images courtesy of Gail Christeson. Part **c** adapted with permission from REF.[50], Wiley.

Box 2 | Scientific outcomes of Expedition 364

In 2016 ICDP-IODP Expedition 364 (site M0077) recovered continuous drill core through the peak ring of the Chicxulub impact structure (FIG. 2) and overlying marine sediments[18,145,146]. This expedition revealed that the peak ring is formed from fractured, highly shocked, granitic basement rocks covered by about 100 m of impactites[18]. The lithology and physical state of the peak-ring rocks helped to differentiate between competing models of large-crater and peak-ring formation[18,68]. For example, shock pressure estimates obtained from shocked minerals within the peak-ring rocks are consistent with numerical simulations of the impact-induced shock wave[18–20,69] (FIG. 1a). Pervasive fracturing of the peak-ring rocks during the passage of the shock wave, as well as acoustic fluidization[73], are likely to be responsible for the transient rock weakening[20] that leads to the collapse of a bowl-shaped transient crater to form a larger, flatter, complex crater (FIG. 1). Core data show that impact-generated, hot hydrothermal fluids passed through the heavily fractured peak-ring rocks for at least 170,000 years, and vented into the ocean above the crater[154]. Venting appears not to have been a hindrance to life, which recovered quickly within the impact basin[21–24]. At some point the peak-ring rocks became a habitat for life, as they now host a living deep biosphere[163]. The transition from impactites to normal marine sedimentation is relatively expanded and intact[55,56], with the global iridium-rich layer (FIG. 5k) recovered at the transition[82].

of a Cenozoic basin[14], where the crater floor is seen to deepen in the annular trough (compare FIG. 2b,c with FIG. 1d), which is consistent with onshore drilling data. Outside this Cenozoic basin, an inward-facing head scarp is observed as an offset in the Cretaceous stratigraphy, and inward-dipping reflectors appear to connect these offsets with a downthrown Moho[49] (FIG. 2a). This is particularly clear along reflection profile Chicx-C, where dipping reflectors are seen to offset the Moho[15]. Although topographic highs across the crater would have been short-lived because of an energetic ocean resurge[49,55,61], the presence of two scarps (rings) a large distance apart and external to the peak ring led to the interpretation that Chicxulub was a multi-ring basin 180–200 km in diameter[14,61]. Chicxulub is also interpreted as a peak-ring crater and/or incipient multi-ring basin 180 km in diameter[34].

The most important parameter for constraining impact energy, however, is the size of the transient crater, which can be approximated by the maximum size of the shock-wave-induced bowl-shape cavity[62] formed after collision (FIG. 1b). Impact energy and angle of impact control the mass, velocity and vaporization of ejected material[63–66] and, thus, the climatic effects of the impact. In reconstructions of the transient crater, megablocks in the terrace zone are moved back to their position in the transient crater rim[14]. From these reconstructions the apparent diameter of the transient crater (diameter at the Earth's pre-impact surface) is estimated to be between 80 km and 100 km (REFS[14,34]) and the impact energy is estimated to be about 5×10^{23} J. In numerical simulations of crater formation, vaporization and ejection of material from the Chicxulub impact site, the transient crater size is held fixed at approximately 90 km in diameter[19,25,63,64,67].

Large crater and peak-ring formation. Distinguishing between hypotheses of large crater formation is important for our understanding of impact cratering processes[68]. As noted in BOX 1, rocks must be weakened to enable an initial bowl-shaped transient crater to collapse and form a relatively flat final crater (FIG. 1).

Early models for the formation of the Chicxulub peak ring were divergent. In one model, the topographic peak ring in the central basin was interpreted as having formed from a breccia unit on top of a thick sheet of impact melt rock[44], whereas in others it was suggested to be formed from uplifted basement rocks[45,47]. The observation that the inner edge of the terrace zone lies below the peak ring was an important finding for ground-truthing models of crater formation. Hydrocode simulations can reproduce this stratigraphic arrangement, with rocks in the zone of central uplift collapsing outwards and ending up above the collapsed transient crater rim[16–18,69,70] (FIG. 1g). The peak-ring rocks recovered at site M0077 (BOX 2) are heavily fractured, uplifted granitic basement rock that have been subjected to high shock pressures, in accordance with hydrocode model predictions[18,20,69]. Jointly, the seismic observations, drilling data and numerical simulations support the dynamic collapse model of crater formation, and suggest that alternative models for peak-ring formation, such as the nested melt-cavity hypothesis[68,71] and breccia floating on a thick melt sheet[34,44], can be ruled out.

The granitic rocks that form the Chicxulub peak ring are pervasively fractured, and these fractures are offset by (ultra-)cataclasites which, in turn, are offset by shear faults[20]. Pervasive grain-scale fracturing is probably a direct result of the passage of the shock wave through the rocks, and this fracturing acts to reduce rock cohesion[72]. According to the dynamic collapse model, the peak-ring rocks have moved many kilometres during crater formation and the associated strain might have been accommodated through the formation of cataclasites[20]. Finally, shear faults indicate that the rocks had regained some strength, and this probably occurred during the final stages of peak-ring emplacement[20]. As noted above, some sort of rock-weakening mechanism is required to explain why rocks temporarily behave as a viscous fluid to produce relatively flat large craters (FIG. 1). Collectively, data from the Chicxulub peak ring suggest that shock-wave induced fracturing and acoustic fluidization[73] are the principal weakening mechanisms[20].

Asymmetries in potential field (gravity and magnetic) data were interpreted in terms of crater structure and used to argue for different angles and directions of impact[74,75]. Subsequently, seismic data revealed that the offshore gravity data were dominated by differences in sedimentary thickness[67], negating some of the arguments for a particular impact direction. Asymmetries in the Chicxulub impact structure are also revealed in seismic data[15], and numerical simulations indicate that differences in pre-impact sedimentary thickness and water depth, as well as obliquity of impact, can both produce asymmetries in final crater structure[19,67]. Whereas the southwest offset of the central uplift was argued to indicate that the direction of impact was towards the northeast[75], this was contraindicated by numerical simulations of crater formation[19]. Asymmetry in Moho topography and central uplift are consistent with an impact angle of between 45° and 60° to the horizontal, and towards the southwest[19].

The impact angle and transient crater size can help us to place constraints on the size and velocity of the

Impact plume
Cloud of gas and fine debris that rapidly expands away from the impact site at high velocity.

Chicxulub impactor. For the same impactor speed and size, the transient crater becomes smaller as the angle of impact becomes more oblique[76]. For an asteroid speed of around 18 km $\mathrm{s^{-1}}$ and impact angles of between 45° and 60°, impactor diameters of around 12.2–14.4 km are required to produce an approximately 90-km-wide transient cavity[64,77,78]. The angle and direction of impact affect the dispersal of ejecta around the globe[63].

Ejecta dispersal

In this section, we review how ejecta leaves the impact site in the ejecta curtain and plume (FIG. 1a,b and BOX 1) and travels around the globe to form the global K–Pg layer. Within a few thousand kilometres of the impact site, the K–Pg boundary contains a layer (or layers) of glassy impact spherules (microtektites)[79], which lie below an iridium-rich layer that also contains shocked minerals. At distal sites (>6,000 km from Chicxulub), only the iridium-rich layer is present. The glassy impact spherules are widely agreed to be formed from impact melt droplets that leave the impact site within the ejecta curtain[80] (FIG. 1a and 3a), but the iridium-rich global K–Pg clay layer is more difficult to explain.

Formation of the global K-Pg layer. It was initially envisaged that impact debris circled the Earth in the stratosphere for several years before settling to the Earth's surface, as ash does in a volcanic cloud[4]. Such a mechanism helps explain the relatively even distribution of ejected debris: the K–Pg clay layer is generally a few millimetres thick at distal sites all around the world[2]. At many distal sites, more than half of the layer is formed from a different type of impact spherules (microkrystites)[81], and both the spherules and surrounding clay have an extra-terrestrial signature[80–82]. Microkrsytites are interpreted as condensates formed in the impact plume[83] ejected at high speed on ballistic trajectories that take them hundreds of kilometres above the Earth's

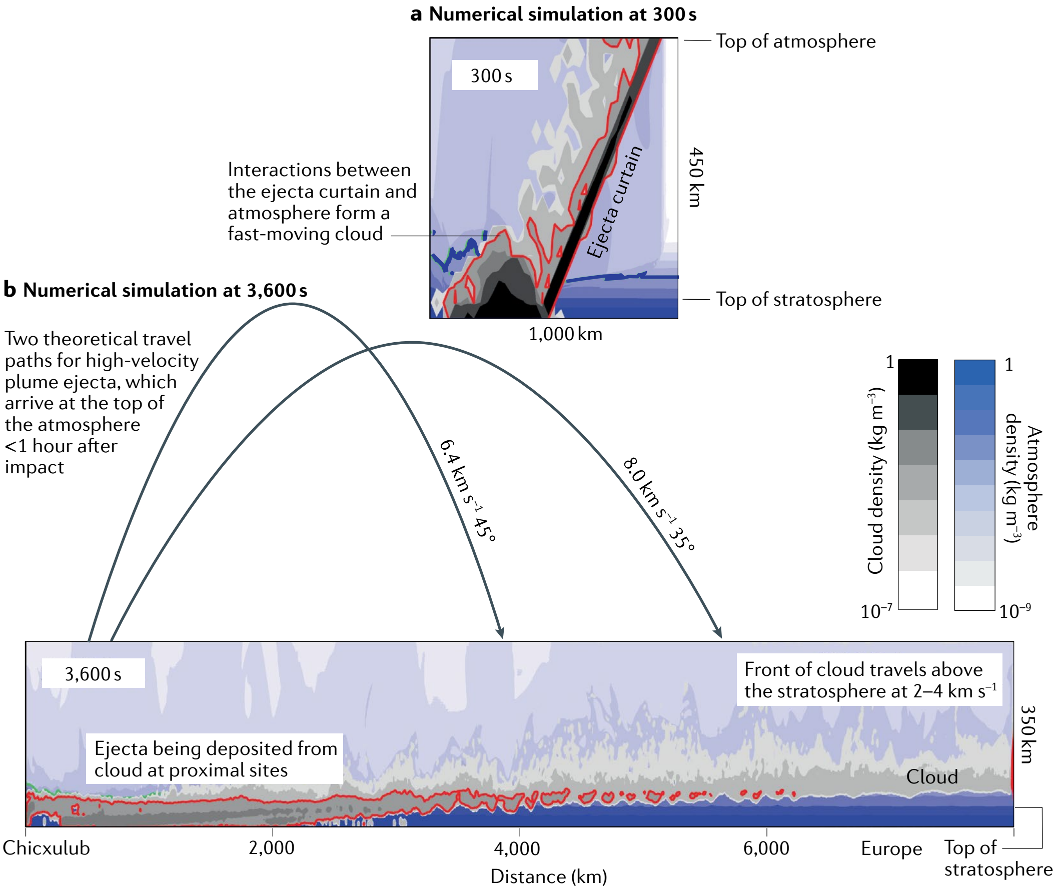

Fig. 3 | **Numerical simulation of the Chicxulub ejecta curtain and its interaction with the Earth's atmosphere.** **a** | 300 seconds after impact[25]. The uppermost part of the ejecta curtain leaves Chicxulub at velocities of >5 km $\mathrm{s^{-1}}$, is vapour-rich, and is principally composed of highly shocked asteroidal and sedimentary rocks. The lower part of the ejecta curtain has been slowed by the atmosphere, leading to its collapse, forming a fast-moving cloud that includes more weakly shocked material, such as shocked quartz from the Chicxulub basement. Red (dust) and blue (atmosphere) lines correspond to a density of 1×10^{-4} kg $\mathrm{m^{-3}}$. **b** | 3,600 s after impact. The ejecta curtain has now completely collapsed and the cloud extends from Chicxulub out to a distance of >8,000 km. Some ejecta are being deposited at sites proximal to Chicxulub, whereas the front of the cloud is still above the stratosphere. Theoretical travel paths show impact plume material (for example, microkrystytes) that are ejected hundreds of kilometres above the Earth and return to the top of the atmosphere after the front of the cloud has passed; these ejecta will become incorporated into the cloud[25]. The cloud transports shocked minerals, soot, dust, and sulfate aerosols from the target rocks, as well as asteroidal material, around the entire globe within 4–5 hours of the impact. Figure adapted with permission from REF.[25], Wiley.

surface[84–88] (FIG. 3b). Although this theory — that material in the global K–Pg layer originates from the impact plume — became widely accepted, it cannot explain some features of the layer, such as why the layer has a relatively constant thickness and contains shocked minerals[25,86].

Shock features would be annealed if ejected at high enough velocity (>7.5 km s^{-1}) to reach distal sites[86], and the impact plume debris would have to be ejected with an extraordinary mass–velocity relationship to ensure that ejecta are distributed evenly around the globe. Numerical simulations of the Chicxulub impact show that oblique impact angles lead to an asymmetric ejection of debris[89] (FIG. 1a), and that most of the ejected mass (80–90%) lies within the ejecta curtain, meaning that there is not enough vapour in the plume to produce all the microkrystites in the distal layer[25]. Also, the basement rocks that sourced the shocked quartz are ejected at too low a velocity (<3 km s^{-1}) to reach distal sites, because of their burial depth >3 km below the pre-impact surface. Hence, a mode of ejecta dispersal that enables ejecta curtain material and shocked basement rocks to reach distal sites is required.

After the Shoemaker–Levy comet collided with Jupiter in 1994, debris was observed to slide around Jupiter on the top of its atmosphere[90], and this was argued to be a result of the deceleration of high-velocity debris heating up the atmosphere[91]. Models of Chicxulub ejecta re-entering the Earth's atmosphere show that ejecta–atmosphere interactions re-distribute ejecta laterally and more evenly[63,92,93]. Interactions between ejecta curtain material and the atmosphere lead to the formation of a fast-moving cloud (FIG. 3a) that is still travelling at 2–4 km s^{-1} at 8,000 km from Chicxulub when the simulation is stopped[25] (FIG. 3b).

Some impact plume ejecta might arrive at the top of the atmosphere before the cloud has arrived, but the majority will arrive after it has passed and become incorporated in the cloud[25]. The velocity of the cloud suggests that it will circle the Earth within 4–5 hours, carrying pulverized solid target rock (dust), soot from heated organic matter at the impact site[94], and sulfate aerosols from the devolatization of sedimentary rocks, which all have climatic effects[26–29,95–99]. This mode of ejecta dispersal enables ejecta curtain material, including shocked minerals, to reach distal sites, and also provides a plausible explanation for the even distribution of the distal ejecta. If this model is correct, the impact spherules were not just formed within the impact plume, they must also have been formed from vapour in the ejecta curtain and/or cloud.

Global wildfires. The finding that ejecta arrives on top of the Earth's atmosphere at one location but ends up being deposited at locations hundreds to thousands of kilometres away has consequences for the ignition of wildfires. Global wildfires are hypothesized to be ignited by radiating ejecta as it re-enters the Earth's atmosphere[85,87,93,100], but these models assume that identical mass fluxes of ejecta arrive all around the globe at the same high velocity (around 8 km s^{-1}). More realistic mass fluxes and velocities, based on hydrocode simulations of ejection from the impact site, indicate that the duration and intensity of thermal radiation varies with distance and direction from the impact site[101]. When tested in a fire-engineering laboratory, modelled radiation pulses[101] were found to be sufficient to ignite fires in some regions[102] but not globally as originally proposed[85]. Widespread fires appear to be necessary, however, to explain the global soot anomaly[100,103,104] even if some soot is derived from organic matter at the impact site[94,99]. The co-location of soot with the iridium anomaly[104] suggests that the soot and the iridium were emplaced over similar timescales. In conclusion, ejecta re-entry models and soot observations are consistent with some wildfires being ignited by re-entering ejecta and some ignited naturally very shortly (weeks to months) after impact. Wildfires can also be started close to the impact site (up to 3,000 km away) as a result of thermal radiation emitted by the impact plume[78,105].

Climatic effects

Dust, sulfate aerosols, CO_2 and soot from target rocks at the impact site, and water vapour from the shallow sea that covered them, along with CO_2 and soot from post-impact wildfires, circled the Earth and determined the climate along with the chemical state of the oceans in the subsequent days to millennia. Dust, sulfate aerosols and soot all lead to a global reduction in temperature and photosynthesis, but the relative and combined effect of these climate forcers is uncertain. Models play a particularly important part in helping us to understand the short-term effects of the impact, as these are difficult to extract from proxy data owing to their limited temporal resolution.

Dust. The hypothesis of an impact winter, defined as the reduction of incoming sunlight over several years, resulting in reduced photosynthesis and severe cooling, was originally proposed to be a consequence of globally distributed pulverized rock (dust)[4]. The effect of dust has been investigated in detail for almost 40 years by radiative, atmospheric–chemical and climate models, combined with theoretical calculations and observations[29,30,95,106–108]. The strength and duration of darkening is difficult to quantify, because several critical parameters, including the total mass of dust, are poorly constrained[109]. The size distribution, coagulation to form larger particles, density and optical properties all control how long dust remains above the Earth's surface[29,108,109].

Although, at one point, silicate dust was ruled out as a primary cause of the impact winter[107], the dust mass was underestimated (at <10^{14} g) in this study, and the dust size was overestimated. The total mass of dust is likely to be orders of magnitude greater (10^{16}–10^{19} g), with large contributions from pulverized sedimentary rock and vapour in the impact plume[109]. The cloud in FIG. 3b is dominantly formed from sedimentary rocks[25], which are expected to fragment into smaller pieces than basement rocks as a result of their porosity[110]. The cloud might also contain iron-rich nanoparticles[109], as these are found in the K–Pg boundary clay[111] and are argued to be formed from condensation in the impact plume. Their total mass, however, is poorly constrained (zero to 10^{18} g)[109]. Two independent climate models, that used the same total dust mass (2×10^{18} g) produced two different post-impact cooling curves (FIG. 4a). In one, the iron-rich nanoparticles coagulated rapidly and fell out after a few months, leading to less darkening than other climate forcers (sulfate aerosol and soot)[29]. In the other, for which the particle-size distribution was based on data from the Tanis K–Pg site in North Dakota, the dust induced ten years or more of darkening and cooling (FIG. 4a), a comparable period to that induced by other climate forcers[30]. The latter study[30] does not include coagulation, however, and so it remains unclear whether dust had a major role in inducing the impact winter.

Sulfate aerosols. The sedimentary rock at the Chicxulub impact site is characterized by a high proportion of the sulphur-rich mineral anhydrite[112], which is subject to vaporization on impact and forms sulfate aerosols after injection into the atmosphere[97]. The climatic effect of sulfate aerosols is short-term cooling and a reduction in precipitation[95–98,113]. More advanced climate models[27–30] show a global annual mean temperature reduction of between 15 °C and 26 °C in the second to fourth year after the impact, and a recovery time of between 15 and 30 years (FIG. 4a–c). A key uncertainty for modelling the climatic effect of sulfate aerosols is the ratio of SO_3 to SO_2 in the impact cloud. Aerosol formation is slower for SO_2, and the aerosol particles are smaller in size, which means they reside for longer in the atmosphere and have a stronger climatic effect[29,97]. Most models have assumed that the proportion of SO_2 is higher than SO_3 (REFS[27–30,97]), but theoretical and experimental evidence indicate that the majority of sulfur in the impact plume is in the form of SO_3 (REF.[114]). If this is correct, sulfate aerosols would form rapidly, and would be more prone to being scavenged by fast-moving silicate particles that settle to the ground on a timescale of days[29,114]. In addition, the coagulation and settling process of the sulfate aerosols could be accelerated by the presence of water vapour originating from the marine impact site, the effect of which has not yet been included in modelling studies investigating the climatic effect of sulfate aerosols[27–29]. Hence, in this scenario, the impact winter would be limited to several months, but the surface ocean would be strongly acidified for several years[114]. Whether the sulfate aerosols remained in the atmosphere for an extended period or not, they are unlikely to have reduced solar radiation below the limit for photosynthesis[29,97].

Soot. Soot from wildfires and organic matter buried at the impact site has the potential to halt photosynthesis for longer than dust and sulfate aerosols[29,30,99]. The optical properties of soot lead to absorption of incoming solar radiation, heating of the atmosphere, and a longer residence time above the Earth's surface[26]. In simulations with a coupled global climate model including atmospheric chemistry, soot reduces solar radiation below the limit for photosynthesis for more than a year, and leads to an average temperature reduction of >20 °C on land[26,30]. Surface temperatures then take 10–15 years to recover to near pre-impact levels[26,29,30] (FIG. 4a). In addition, the cool temperatures weaken the hydrological cycle and reduce global average precipitation by 70% to 80% relative to pre-impact levels for at least six years[26]. The inclusion of water vapour from the marine impact site only slightly attenuates the radiative effect of soot in the months immediately following impact[26]. Wildfires are likely to burn for weeks to months, so the emplacement of wildfire soot in the stratosphere will occur over an extended period, whereas soot generated at the impact site would have an immediate effect[94].

Post-impact temperatures from three independent climate simulations (FIG. 4a) show comparable trends, magnitudes and recovery times. Specifics of the climate model and/or input parameters might be able to explain the differences in detail, but uncertainties remain as to which climate forcer had the strongest effect.

Productivity changes in the post-impact oceans. Although, as discussed above, silicate dust might not have played a major part in the impact winter, it is rich in iron, which, when dissolved in the ocean, would have been a source of nutrients. Nutrient levels would have also been increased by the upwelling induced by surface ocean cooling[27,28]. Simulations with a three-dimensional ocean biogeochemistry model coupled to an intermediate-complexity atmosphere–ocean model[28] show that, after a short collapse of ocean net primary productivity (NPP) caused by the cool and dark conditions in the first few years post-impact, surface water nutrient levels increased, leading to a decade-long increase in primary productivity (FIG. 4d,e). Aerosols from wildfires can also increase nutrient levels[115], which could have further increased marine productivity.

Carbon dioxide. A longer-term increase in CO_2 can be attributed to the addition of large amounts of carbon from the target rock, the burning of terrestrial organic material and soil decay[116]. This led to warming after the impact winter that lasted for around 100,000 years.

One of the effects of a modelled increase in marine NPP[28] is that it increases carbon uptake of the ocean, which then weakens the global warming. Assuming a late-Cretaceous atmospheric CO_2 concentration of about 500 ppm (REF.[28]), simulations testing different amounts of carbon emplaced in the atmosphere after the impact indicate that around 1,500 Gt carbon is required to explain the long-term warming of 1–2 °C (REFS[117,118]) indicated by proxy data; see below. In this case, the increase in atmospheric CO_2 concentration is about 350 ppm after approximately 1,000 years, when the carbon exchange between ocean and atmosphere is largely in equilibrium. This increase of the post-impact atmospheric CO_2 concentration falls within the range suggested by a CO_2 reconstruction based on leaf gas-exchange principles[119]. If around 1,500 Gt carbon had been released as a consequence of impact, a large mass of carbon must have originated from terrestrial fires and/or soil decay, because the mass of carbon injected into the atmosphere from target rocks at the impact site is unlikely to have exceeded 160 Gt (REF.[64]). Higher pre-impact atmospheric CO_2 concentrations would require even higher additional C masses to cause the same warming.

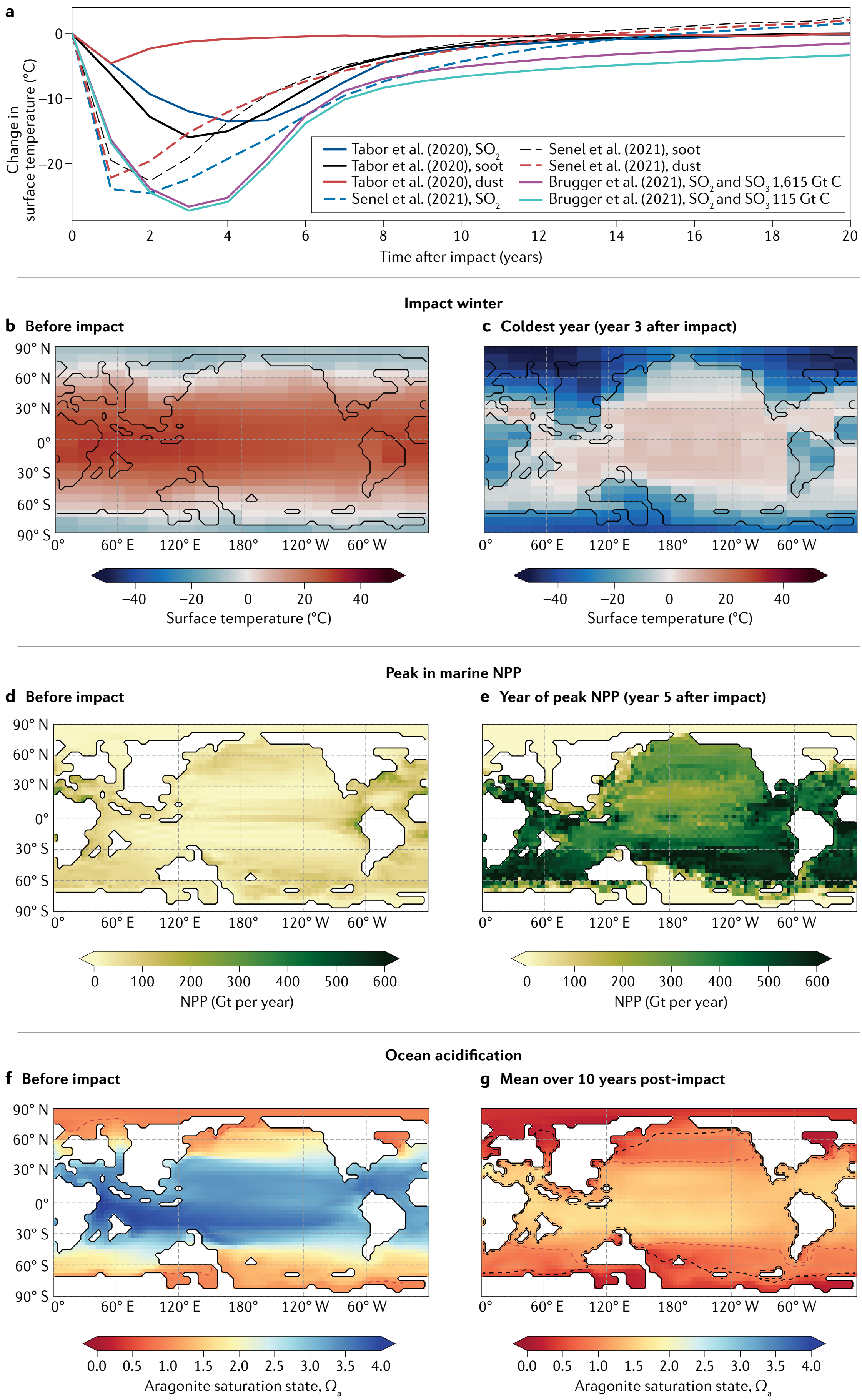
a
0
−10
−20
Change in surface temperature (°C)
0
2
4
6
8
10
12
14
16
18
20
Time after impact (years)
Tabor et al. (2020), SO_2
Tabor et al. (2020), soot
Tabor et al. (2020), dust
Senel et al. (2021), SO_2
Senel et al. (2021), soot
Senel et al. (2021), dust
Brugger et al. (2021), SO_2 and SO_3 1,615 Gt C
Brugger et al. (2021), SO_2 and SO_3 115 Gt C
Impact winter
b Before impact
c Coldest year (year 3 after impact)
90° N
60° N
30° N
0°
30° S
60° S
90° S
0°
60° E
120° E
180°
120° W
60° W
−40
−20
0
20
40
Surface temperature (°C)
Peak in marine NPP
d Before impact
e Year of peak NPP (year 5 after impact)
0
100
200
300
400
500
600
NPP (Gt per year)
Ocean acidification
f Before impact
g Mean over 10 years post-impact
0.0
0.5
1.0
1.5
2.0
2.5
3.0
3.5
4.0
Aragonite saturation state, Ω_a

◄ Fig. 4 | **Modelled pre- and post-impact climate and ocean chemistry.** Climate simulations reveal the severity of the impact winter and adverse environmental changes in the oceans. **a** | Surface temperature change after the impact for sulfate aerosols (blue), soot (black) and dust (red), as modelled in REFS[29,30], compared to simulations including sulfate aerosols and carbon[28] (magenta and cyan). **b–g** | Maps of different variables before and after the impact, as modelled in REF.[28]. **b** | Surface air temperature before the impact. **c** | Surface air temperature in year 3 after the impact, the year of minimum global mean temperature. **d** | Marine net primary productivity (NPP) before the impact. **e** | Marine NPP in year 5 after the impact, the year of peak ocean productivity. **f** | Aragonite saturation state, as a measure of ocean acidification, before the impact. Calcifying species begin to dissolve at $\Omega_a < 1$; the red line shows $\Omega_a = 1$. **g** | Aragonite saturation state, averaged over the 10 years after the impact. The red line shows $\Omega_a = 1$ for the ten-year average. The black line shows $\Omega_a = 1$ at 1,000 years after the impact. Parts **b–g** adapted from REF.[28], CC BY 4.0 (https://creativecommons.org/licenses/by/4.0/).

Climatic conditions after the impact winter, characterized by increased temperatures and higher atmospheric CO_2 concentrations, also resulted in an increase of terrestrial NPP[120]. This has contributed to the recovery of carbon storage in vegetation biomass and would have led to a drawdown of atmospheric CO_2 concentrations, possibly on a timescale of about 100 years[120].

Proxy record of impact-induced climatic and oceanographic changes. The impact winter and other immediate effects of the impact happened so geologically rapidly that they are difficult to identify from K–Pg boundary sequences. However, unusually rapid deposition in unique settings has yielded proxy records of the decades to millennia after the impact and these data are important for examining the validity of model simulations of the post-impact climate. Dramatic cooling of the Earth's surface leads to a reduction in upper ocean temperature. TEX_{86} data, based on the analysis of marine Thaumarchaeota, can resolve past changes in sea-surface temperatures. These data indicate a pronounced short-term surface ocean cooling of 6–7 °C in the months to decades after the impact for the Brazos River section, Texas and the New Jersey palaeoshelf[117,121], consistent with the results of climate model simulations[26,27,29]. In addition, in the Geulhemmerberg section in The Netherlands, a small decrease in pH (0.25) is observed in boron isotope measurements from directly above the K–Pg boundary[122], consistent with models including the marine carbon cycle that suggest rapid (less than 1,000 years after the impact) but relatively minor surface ocean acidification following the impact[28,122] (FIG. 4f,g). Although both of these signals are impossible to date precisely for different reasons, their relationship with the K–Pg boundary depositional sequence and other impact-related markers strongly suggests deposition within the first century (Brazos and New Jersey)[117,121] to millennium (Geulhemmerberg)[122] after the impact. Finally, TEX_{86} data from several locations also show a longer-term warming of 1–2 °C compared to the pre-impact temperatures in the centuries to millennia after the impact[117,118].

Ecological and environmental implications

Severe short-term cooling and darkening, a reduction in precipitation, widespread terrestrial wildfires, and, to a lesser degree, ocean acidification, all potentially influenced which species went extinct. A long continuous cold period, with temperatures staying below freezing for several years in most regions[26,27,29,30], would have contributed to harsh living conditions. The combination of reduced light levels and precipitation made it difficult for plants to grow, and ocean acidification is potentially disastrous for calcifying organisms in surface waters. Additionally, a few years after the impact, ozone depletion occurred as a consequence of soot in the stratosphere, which would have posed a severe threat for species sensitive to ultraviolet radiation[26,123].

The K–Pg mass extinction was strongly selective with freshwater and terrestrial species generally hit less severely than marine species[124–126], surface-dwelling marine species hit harder than deep-dwelling marine species[127], detritus-feeding organisms hit less drastically than those with other feeding strategies[128,129], and organisms that could shelter underground or in water hit less severely than those that could not shelter[130]. The overall biotic perturbation was so strong that it took ecosystem function and biogeochemical cycles several million years to recover[126]. These long-term effects have been studied in considerable detail in palaeontological and proxy records from numerous lower-Palaeocene deep-sea sections[3,131,132].

Extinction mechanisms. Previously proposed extinction mechanisms can be compared with model simulations of the immediate post-impact environment. Numerous mechanisms have been proposed for the extinction of the calcareous plankton, including darkness and impact winter, ocean acidification[116,126,133,134], and heavy-metal poisoning[135] (see summaries in REFS[3,124,126]). The climate simulations shown in FIG. 4 suggest that the impact winter lasted about a decade. Although phytoplankton can survive short intervals of darkness, it is likely that months of darkness combined with extreme cold would have killed a large proportion of phytoplankton species, with cyst-forming taxa or those with vegetative stages having higher chances of survival[136–139]. Decimation of the base of the food chain would have affected higher trophic levels, including invertebrates (bivalve and ammonite molluscs), grazers (including copepods and shrimp) and fish, although fish had regionally low extinction rates[140]. On land, the impact winter and fire led to destruction of vegetation, including a decrease in plant diversity[141], diminishing the supply of food for terrestrial organisms[141]. These effects would have made species such as the dinosaurs that were dependent on primary production more susceptible to extinction than detritus feeders, including many mammals[125,129,142], although other potential killing mechanisms exist[130].

Ocean acidification was less drastic because of the large buffering capacity of the surface ocean[143,144] and simulations (that do not consider rapid sulfate deposition) suggest a modest 0.4 decrease in pH[28], which is consistent with proxy data[122]. This is not large enough to explain the near-global extinction of planktic foraminifera and nannoplankton[28,116]. However, on a regional level, ocean acidification might have contributed to the extinction of certain calcifiers[28,114] especially those such as the ammonites and belemnites that made shells from aragonite (the more solution-susceptible polymorph of $CaCO_3$). Ocean acidification might have been more severe if sulfates were deposited more rapidly[28,114], as discussed above.

Expanded marine K–Pg sections at Brazos, Texas, the New Jersey palaeoshelf, and terrestrial sequences in the western USA and elsewhere remain our best opportunities for teasing out climatic changes, extinction mechanisms and reasons for survivorship. As shown, these expanded sections enable the detection of evidence for the environmental effects from model results[27,28] in the rock record, but examination of their relationship with the extinctions and recovery is limited by the quality of the palaeontological record.

Record at the impact site

A relatively expanded transition from crater rocks to normal marine sedimentation was recovered in the Chicxulub impact structure at site M0077 (FIGS 2 and 5). In this section we describe the stratigraphy and lithology across this transition, recovery of life at the impact site, as well as the discovery that the peak-ring rocks host a living deep biosphere.

Lithology and stratigraphy of site M0077 in the Chicxulub crater. The uppermost peak-ring is formed from cross-bedded gravel- and sand-sized suevite, and covered by the so-called transitional unit (units 2A and 1G[145,146]) (FIG. 5k). The transitional unit is a 75-cm-thick dark-brown, fining-upward silt- and clay-sized limestone that marks the transition from impactites to normal marine sedimentation[21,55,56]. At the top of the transitional unit is a 4-cm-thick grey-green marlstone that represents the onset of hemipelagic deposition in the newly formed crater (FIG. 5k). Deposition of the uppermost suevite unit at site M0077 (unit 2A in FIG. 5k) probably lasted hours or days after impact at most, and deposition of the transitional unit (unit 1G) took place over days to months, or at most a few years (FIG. 5k), as suggested by He isotope data[21,23]. This record provides unprecedented detail of the events during the hours to days to millennia as energy from the impact subsided, ocean waters filled the crater, and life explored this unique environment[3,21–23,55,56,147].

In terms of duration, the deposition of the green marlstone layer above the transitional unit is the most contentious (FIG. 5k). There are two end-member age models: a rapid scenario (FIG. 5l) in which the marlstone was deposited within months to a few years after impact, and a slow scenario (FIG. 5m) in which deposition occurred over millennia to several tens of millennia. The rapid age scenario is based on interpretation of the iridium anomaly, which occurs in the uppermost part of the transitional unit and peaks in the green marlstone[82] (FIG. 5k). This traditional interpretation of the iridium anomaly — that it represents atmospheric fallout over months to a few years after impact — is supported by the occurrence of a potential airfall charcoal layer (FIG. 5a,b) at the top of the green marlstone[23,55]. The slow scenario is based on planktic foraminiferal biostratigraphy with the lowermost Pα zone representing 30,000 years in traditional zonations, determined using the assumption of constant sedimentation rates within magnetic polarity zone C29r[21,148]. The iridium anomaly (FIG. 5k) might have been redistributed after burial by reducing pore waters[23,82] and assumptions of constant sedimentation rates over tens of millennia are unlikely, especially in the rapidly changing post-impact environment[23]. Thus, the true age model for deposition of the marlstone layer is likely to be somewhere between the rapid and slow end-member models.

Pα zone
Interval defined by the total range of the planktonic foraminifer *Parvulorugoglobigerina eugubina.*

Fossil record of site M0077. The transitional unit, and especially the green marlstone unit, contain a rich mineral and molecular fossil record, composed mostly of prokaryotes and eukaryotic protistans. Although most of the molecular and mineral fossils in the transitional unit are Cretaceous, a narrow interval at the base of the transitional unit contains relatively common nannoplankton and dinoflagellate cyst species that survived the impact at other locations (FIG. 5i,j). The relative abundance of these species suggests that they might be the first life to re-enter the crater, probably swept in by tsunami[23]. Planktic foraminiferal assemblages in the uppermost two decimetres of the transitional unit, which was deposited slowly compared to the rest of the unit, are composed of species also known to survive the boundary, which is indisputable evidence for the return of life to this new habitat[21]. The same interval and the green marlstone unit above contain trace fossils, suggesting that rapid recolonization of the seabed by benthic invertebrates occurred at the same time as the crater sea surface became inhabited[147].

The green marlstone contains a comparatively rich fossil record, most notably the first Palaeocene foraminiferal species[21], and a nannoplankton assemblage almost completely dominated by calcareous dinoflagellate resting cysts belonging to the genus *Cervisiella*[23] (FIG. 5g). Cysts represent a strategy by which plankton could escape harmful surface ocean environments, and cyst-bearing species are known to have selectively survived the extinction[126]. This contrast of moderately diverse planktic foraminifera but depauperate nannoplankton is observed at numerous other locations around the world[149] and suggests that the ocean surface remained unsuitable for phytoplankton but that there was a plentiful food supply for zooplankton. Biomarkers in the green marlstone are diagnostic of a thriving unicellular cyanobacterial community[22], and it is likely that microbes served as the food supply for the recovering foraminifera[23,150].

A thin layer in the middle of the green marlstone unit contains a diverse array of phosphatic fossils, which resemble appendages of copepods (minute, swimming crustaceans), coprolites (fossilized faecal pellets) and small fish[23] (FIG. 5c–f). Such a rich array of fossils would be unusual for any geological interval but it is unique for the immediate post-impact interval. This thin treasure trove of fossil preservation, a microscopic Konservat Lagerstätten[151–153], represents a unique environment in the nascent crater, probably a combination of elevated surface ocean nutrients suggested by the concentration of phosphate in models, which is consistent with the abundance of cyanobacteria, combined with pore water euxinia, ideal for preservation. The timescale of recovery of nannoplankton, slowed by harmful surface oceans, is consistent with the rapid age scenario, as it would be unrealistic for such harmful surface ocean

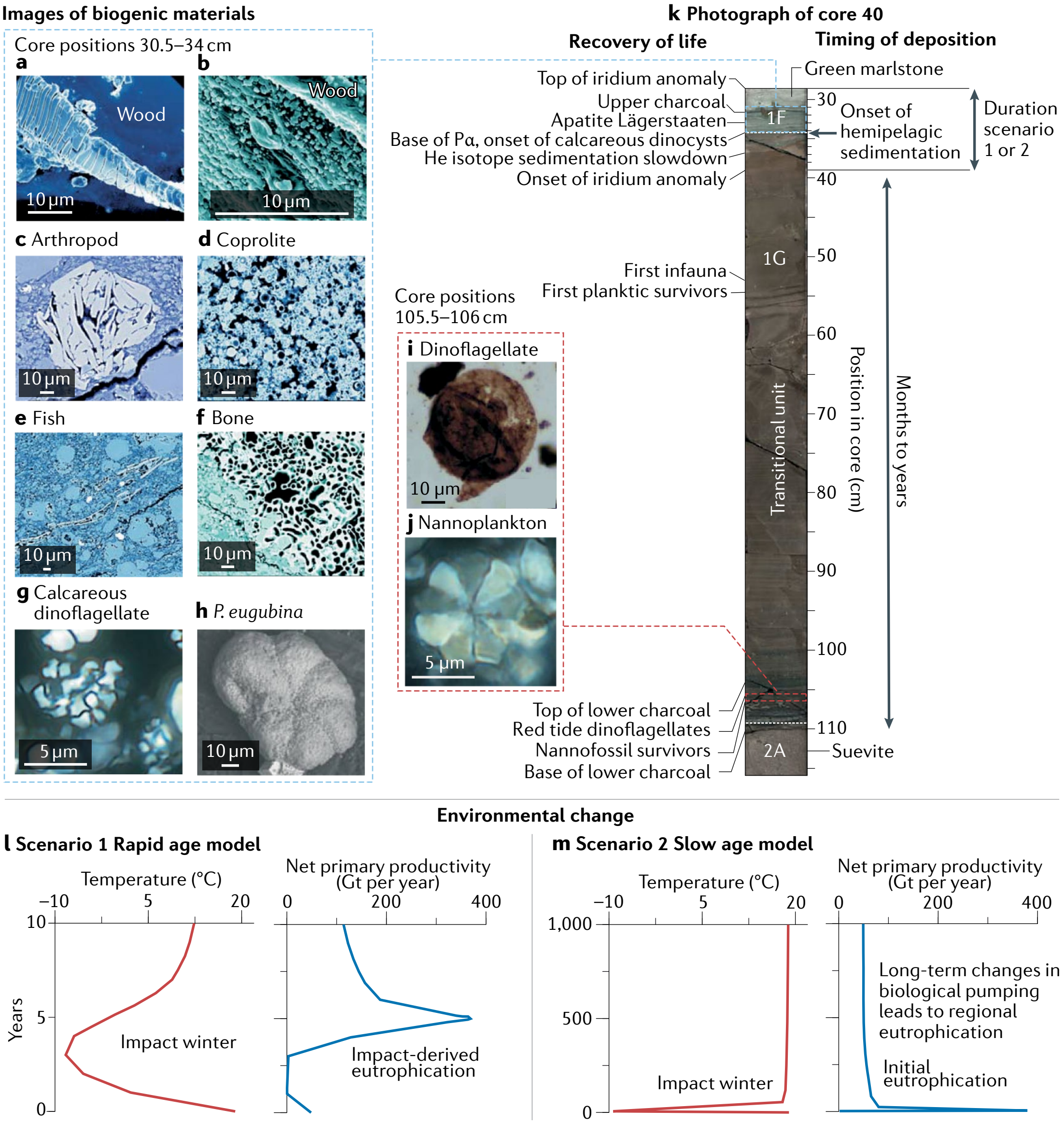

Fig. 5 | **Sediment and fossil record at the Chicxulub impact site. a–j** | Images of biogenic materials at various core depths: **a** | Petrified wood (31 cm). **b** | Wood covered with halite (33 cm). **c** | Marine arthropod (32–34 cm). **d** | Fossilized bacteria in coprolite (32–34 cm). **e** | Possible fish fossil (32–34 cm). **f** | Bone tunnelled by cyanobacteria (32–34 cm). **g** | Calcareous dinoflagellate *Cervisiella* spp. (30.5 cm). **h** | Planktic foraminifer *Parvularugoglobigerina eugubina* (31–32 cm). **i** | Dinoflagellate survivor *Trithyrodinium evittii* (106 cm). **j** | Survivor nannoplankton *Biantholithus sparsus* (105.5 cm). **k** | Photo of core 0077A-40R-1 from IODP-ICDP Expedition 364 showing: the transitional unit (unit 1G) deposited by seiche waves over months to years[55], named for its transition in depositional mode and timing from the underlying suevite (unit 2A, high-energy seiches and tsunami deposited over hours and days) and overlying green marlstone (unit 1F, hemipelagic deposition over much longer time spans, see discussion)[21,56]. The transitional unit is a brown-coloured fine carbonate-rich mudstone, which is gradational over a few centimetres with the underlying suevite but largely distinct from the overlying green marlstone. The onset of the iridium anomaly constrains the deposition time of the transitional unit below 39 cm to be no more than a few years. **l**, **m** | Above 39 cm there are two end-member scenarios: a rapid age scenario in part **l** and a slow age scenario in part **m**. Model results for ocean net primary productivity and temperature (from Brugger et al.[28], 115 Gt carbon, 100 Gt sulphur, the effect of silicate dust on the ocean included) plotted using the rapid age scenario (part **l**) and the slow age scenario (part **m**). The transitional unit records the return of life in the ocean above the impact crater. Part **k** (core photo) is adapted from REF.[146], CC BY 4.0 (https://creativecommons.org/licenses/by/4.0/).

environments to have persisted for millennia. The increase in productivity in the green marlstone is also consistent with model predictions[28] if the rapid age model is correct (FIGS 4e and 5l), although an extended interval of enhanced productivity might also be related to hydrothermal activity at the impact site[23,154].

Environmental record from site M0077. Nutrification of the ocean after the impact-induced darkness is observed in the Ba proxy record at Site M0077. Ba/Ti increases in the green marlstone but peaks in the overlying lower Danian limestone[21]. Ba signals from distal sites suggest a regionally variable but longer-term interval of post-impact high export productivity[149] consistent with interpretation of benthic foraminiferal assemblages[155]. The short-term, post-impact nutrification spike was not a kill mechanism, but it was extended by the changing nature of biological pumping and chemical cycling to become a long-term response of the mass extinction[126,139,150] with profound impacts on the recovery of life[3,24,156–158]. Moreover, the combined cyst and cyanobacterial record from the green marlstone suggests a structurally different surface ocean community, decades to millennia after the impact, consistent with other locations[159]. These changes are at least partially reflected in the collapse of the traditional vertical carbon isotope gradient[139,160].

Regardless of the timescale of the immediate impact aftermath, cratering processes had a lasting effect on bacterial communities at the impact site (BOX 2). The profound impact of events at the K–Pg boundary in restructuring bacterial communities is also observed at higher trophic levels including calcareous plankton, land plants and vertebrates[141,161,162].

Deep biosphere at Chicxulub. Modern microbial communities sampled from fluids and rocks show discrete enrichments that correlate with lithology. Suevites in unit 2A show particularly elevated microbial abundances compared to surrounding lithologies, suggesting that the cratering process created a favourable substrate for bacteria. The flow of fluids during deposition and in the subsequent hours and days probably created the availability of nutrients and energy for microbial colonization[163]. The underlying suevites (units 2B and 2C), and especially the granite (unit 1) and Cenozoic sediments generally contain much lower microbial abundances. Regardless of the abundance, molecular analyses show that different units contain taxonomically distinct bacterial communities, possibly with different metabolic traits[163]. The heterogeneity of the microbial communities in the deformed target and post-impact rocks suggest that the impact had a major effect on the deep biosphere that continues till the present day.

In summary, the Chicxulub impact caused environmental upheaval that altered the trajectory of life globally. It is possible that cyanobacteria and other microbes that were favoured by the harsh, immediate post-impact oceans[22,159,164] are at least partially responsible for profoundly changing the nature of biogeochemical cycling, which enabled the survival of benthic organisms and grazers and the rapid recovery of fish and zooplankton, but became a barrier to the evolution of new Palaeocene nannoplankton species. The exquisite fossil and biomarker record indicates that the crater became home for a diverse cross-section of life from bacteria to fish within decades to millennia, though the taxonomic composition and structure of ecosystems were profoundly and permanently transformed[22,23,164].

Summary and future perspectives

The Chicxulub impact structure is the best preserved large-impact basin on the Earth, and has proved vital in providing three-dimensional insight into how an impact of this size produces subsurface structural deformation all the way down to the Moho. Structural details such as the extent of the megablock zone below the peak ring serve as important constraints for numerical models of crater formation, which enable the impactor size or, more precisely, its kinetic energy, to be estimated from the size of an impact basin. Impact energy is key to quantifying the impact's environmental consequences[64,96,97], and it also helps us to better estimate the size of impactors that formed basin structures on the Moon (FIG. 1c–h) and other planetary bodies. The reconstruction of the bombardment history of the inner Solar System from the basin record on the Moon allows for a better understanding of how large cosmic bodies impacting the Earth–Moon system shaped the evolution of our planet to become a habitable world. In addition, the crater record on planetary bodies can be understood as a diagnostic tool with which to probe their subsurface properties. This requires a deep understanding of the relationship between observational features, such as crater morphology and size, and the properties of the impacted matter. For example, studies of size-dependent crater morphologies on icy worlds have been used to constrain their near-surface composition[165] and ice-layer thickness[166].

It remains unclear as to exactly where impact spherules (microkrystites) in the global K–Pg layer are formed, but some microkrystites must be formed from ejecta curtain material[25]. Interestingly, there are three texturally and compositionally distinct types of impact spherules in a distal K–Pg layer in Italy, and the glauconite impact spherules at this site are similar to microtektites at proximal sites, which are widely agreed to be ejecta curtain deposits[80]. It is hard to explain, however, why the average size and number of spherules in the layer are similar everywhere[81]. In simulations of the cloud (see, for example, FIG. 3) the larger particles fall out first[25], which is in accordance with the observed decrease in size of shocked minerals in the K–Pg layer with distance from the Chicxulub crater[107]. An observation that might help shed light on where and how spherules are formed is the difference in composition of spinel within impact spherules at sites in the Pacific Ocean, Europe and the Atlantic Ocean[167,168]. Further modelling of impact spherule formation, as well as more analyses of different spherule types (as, for example, in REF.[80]) in other K–Pg sites around the globe might help us resolve where microkrystites are formed.

Uncertainties in the severity and duration of the impact winter remain, although most models now suggest that there was at least a decade of cooling and darkening[26,27,29,30]. Climate models are advancing, and are now able to simulate the combined climatic effect of multiple stressors, by using complex coupled atmosphere–ocean models and by including marine biogeochemical cycling. Adding ecological models makes it possible to simulate the effect on life. For example, the warming effects of CO_2 might have reduced the severity of the impact winter and extinctions on land[113], and dissolved silicate dust and ocean upwelling briefly increased ocean productivity[28].

Future simulations with an atmospheric chemistry model could explore the combined effect of climatically active gases, including the effect of feedbacks. Furthermore, climate model simulations could address some of the current uncertainties by applying the latest knowledge regarding several climate forcers. For example, the simulations could include soot[94] from the target rocks, as well as soot from wildfires over an extended period of several months. Better quantification of the mass, origin (from vapour, sedimentary or basement debris) and size distribution of dust, for example, might also help us to improve climate simulations[30,109]. Ejecta–atmosphere interactions dramatically disturb and heat the atmosphere[25], which will have an effect on particle interactions and behaviour. Hence, ideally, it would be better to couple dust-cloud simulations with global climate models. These, and other factors noted above, mean that uncertainties remain in the residence times of particles in the Earth's atmosphere and, thus, the relative climatic effects of dust, soot and sulfate aerosols.

There is also still substantial uncertainty about the exact cause and timing of the K–Pg mass extinction. Novel proxies, such as clumped isotopes and TEX_{86}, may well expand our understanding of the immediate post-extinction environment and enable us to test various climate model scenarios. Such proxies can be applied broadly because they do not rely on assumptions about the isotopic composition of sea water, as traditional foraminiferal-based stable isotopes do, thus allowing a more detailed understanding of post-impact climate. The extinction was highly selective, and understanding survival is key to unravelling the killing mechanisms. This information is particularly elusive because of the generally condensed nature of most palaeontological records compared to the rapid pace of the mass extinction. More expanded records from Chicxulub[21,23] and elsewhere[169] indicate that higher-resolution timing of the mass extinction can be teased from records. Such records might provide data on, for example, population changes in the immediate aftermath of the impact, and whether higher trophic levels were affected later than species at the base of the food chain. If darkness and impact winter were the leading causes of the extinction, high-latitude species should have been better adapted and should have preferentially survived, and, indeed, the few records available suggest that this is the case[170]. There is a similar paucity of records for freshwater environments, where rates of survival appear to have been higher[125]. Expanded high-latitude terrestrial and marine sequences and freshwater sections would provide a much fuller palaeontological picture of the boundary, with detail on the timing of the extinction and the ecology of surviving species.

1. Russell, D. A. The enigma of the extinction of the dinosaurs. *Ann. Rev. Earth Planet. Sci.* **7**, 163–182 (1979).
2. Schulte, P. et al. The Chicxulub asteroid impact and mass extinction at the Cretaceous–Paleogene boundary. *Science* **327**, 1214–1218 (2010).
3. Lowery, C. M., Bown, P. R., Fraass, A. J. & Hull, P. M. Ecological response of plankton to environmental change: thresholds for extinction. *Ann. Rev. Earth Planet. Sci.* **48**, 403–429 (2020).
4. Alvarez, L. W., Alvarez, W., Asaro, F. & Michel, H. V. Extraterrestrial cause for the Cretaceous–Tertiary extinction. *Science* **208**, 1095–1108 (1980).
5. Smit, J. & Hertogen, J. An extraterrestrial event at the Cretaceous–Tertiary boundary. *Nature* **285**, 198–200 (1980).
6. Byrnes, J. S. & Karlstrom, L. Anomalous K–Pg–aged seafloor attributed to impact-induced mid-ocean ridge magmatism. *Sci. Adv.* **4**, eaao2994 (2018).
7. Schoene, B. et al. U–Pb geochronology of the Deccan Traps and relation to the end-Cretaceous mass extinction. *Science* **347**, 182–184 (2015).
8. Hull, P. M. et al. On impact and volcanism across the Cretaceous–Paleogene boundary. *Science* **367**, 266–272 (2020).
9. Renne, P. R. et al. Time scales of critical events around the Cretaceous–Paleogene boundary. *Science* **339**, 684–687 (2013).
10. Norris, R. D., Huber, B. T. & Self-Trail, B. T. Synchroneity of the K–T oceanic mass extinction and meteorite impact: Blake Nose, western North. *Atlantic. Geol.* **27**, 419 (1999).
11. MacLeod, K. G., Whitney, D. L., Huber, B. T. & Koeberl, C. Impact and extinction in remarkably complete Cretaceous–Tertiary boundary sections from Demerara Rise, tropical western North Atlantic. *Geol. Soc. Am. Bull.* **119**, 101 (2007).
12. Melosh, H. J. *Impact Cratering: A Geologic Process* (Oxford Univ. Press, 1989).
13. Camargo-Zanoguera, A. & Suarez-Reynoso, G. Evidencia sismica del crater impacto de Chicxulub. *G. Bol. Asoc. Mex. Geof. Expl.* **34**, 1–28 (1994).
14. Morgan, J. V. et al. Size and morphology of the Chicxulub impact crater. *Nature* **390**, 472–476 (1997).
15. Gulick, S. P. S. et al. Importance of pre-impact crustal structure for the asymmetry of the Chicxulub impact crater. *Nat. Geosci.* **1**, 131–135 (2008).
16. Morgan, J. V. et al. Peak-ring formation in large impact craters. *Earth Planet. Sci. Lett.* **183**, 347–354 (2000).
17. Collins, G., Melosh, H. J., Morgan, J. V. & Warner, M. R. Hydrocode simulations of Chicxulub crater collapse and peak-ring formation. *Icarus* **157**, 24–33 (2002).
18. Morgan, J. V. et al. The formation of peak rings in large impact craters. *Science* **354**, 878–882 (2016).
19. Collins, G. S. et al. A steeply-inclined trajectory for the Chicxulub impact. *Nat. Comm.* **11**, 1480 (2020).
20. Riller, U. et al. Rock fluidization during peak-ring formation of large impact structures. *Nature* **562**, 511–518 (2018).
21. Lowery, C. M. et al. Rapid recovery of life at ground zero of the end-Cretaceous mass extinction. *Nature* **558**, 288–291 (2018).
22. Schaefer, B. et al. Microbial life in the nascent Chicxulub crater. *Geology* **48**, 328–332 (2020).
23. Bralower, T. J. et al. The habitat of the nascent Chicxulub crater. *AGU Adv*. **1**, e2020AV000208 (2020).
24. Jones, H. L., Lowery, C. M. & Bralower, T. J. Calcareous nannoplankton "boom-bust" successions in the Cretaceous–Paleogene (K–Pg) impact crater suggests ecological experimentation at "ground zero". *Geology* **47**, 753–756 (2019).
25. Artemieva, N. & Morgan, J. Global K–Pg layer deposited from a dust cloud. *Geophys. Res. Lett.* **47**, 1–8 (2020).
26. Bardeen, C. G., Garcia, R. R., Toon, O. B. & Conley, A. J. On transient climate change at the Cretaceous–Paleogene boundary due to atmospheric soot injections. *Proc. Natl Acad. Sci. USA* **114**, E7415–E7424 (2017).
27. Brugger, J., Feulner, G. & Petri, S. Baby, it's cold outside: climate model simulations of the effects of the asteroid impact at the end of the Cretaceous. *Geophys. Res. Lett.* **44**, 419–427 (2017).
28. Brugger, J., Feulner, G., Hofmann, M. & Petri, S. A pronounced spike in ocean productivity triggered by the Chicxulub impact. *Geophys. Res. Lett.* **48**, e2020GL092260 (2021).
29. Tabor, C. R., Bardeen, C. G., Otto-Bliesner, B. L., Garcia, R. R. & Toon, O. B. Causes and climatic consequences of the impact winter at the Cretaceous–Paleogene boundary. *Geophys. Res. Lett.* **47**, e60121 (2020).
30. Senel, C. et al. Relative roles of impact-generated aerosols on photosynthetic activity following the Chicxulub asteroid impact. *GSA Connects* **53**, 6 (2021); https://doi.org/10.1130/abs/2021AM-368627
31. Stöffler, D. et al. Cratering history and lunar chronology. *Rev. Mineral. Geochem.* **60**, 519–596 (2006).
32. Grieve, R. A. F. & Head, J. W. Impact cratering, a geological process on the planets. *Episodes* **4**, 3–9 (1981).
33. Kenkmann, K. The terrestrial impact crater record: a statistical analysis of morphologies, structures, ages, lithologies, and more. *Meteorit. Planet. Sci.* **56**, 1024–1070 (2021).
34. Hildebrand, A. R. et al. Mapping Chicxulub crater structure with gravity and seismic reflection data. *Geol. Soc. Lond. Spec. Publ.* **140**, 153–173 (1998).
35. Alexopoulus, J. S. & McKinnon, W. B. Multiringed impact craters on venus: an overview from Arecibo and Venera images and initial Magellan data. *Icarus* **100**, 347–363 (1992).
36. Alexopoulos, J. & McKinnon, W. B. Large impact craters and basins on Venus, with implications for ring mechanics on the terrestrial planets. *Geol. Soc. Am. Spec. Pap.* **293**, 29–50 (1994).
37. Kyte, F. T., Zhou, Z. & Wasson, J. T. Siderophile-enriched sediments from the Cretaceous–Tertiary boundary. *Nature* **288**, 651–656 (1980).
38. Bohor, B., Foord, E. E., Modreski, P. J. & Triplehorn, D. M. Mineralogic evidence for an impact event at the Cretaceous–Tertiary boundary. *Science* **224**, 867–869 (1984).
39. Stöffler, D., Hamann, C. & Metzler, K. Shock metamorphism of planetary silicate rocks and sediments: Proposal for an updated classification system. *Meteorit. Planet. Sci.* **53**, 5–49 (2018).
40. French, B. M. & Koeberl, C. The convincing identification of terrestrial meteorite impact structures: what works, what doesn't, and why. *Earth Sci. Rev.* **98**, 123–170 (2010).
41. Bohor, B. F. & Izett, G. A. Worldwide size distribution of shocked quartz at the K/T boundary: evidence for a North American impact site. *Lunar Planet. Sci.* **17**, 68–69 (1986).
42. Hildebrand, A. R. et al. Chicxulub crater: a possible cretaceous/tertiary boundary impact crater on the Yucatán Peninsula, Mexico. *Geology* **19**, 867–871 (1991).
43. Swisher, C. C. et al. Coeval ^{40}Ar/^{39}Ar ages of 65.0 million years ago from Chicxulub crater melt rock and Cretaceous–Tertiary boundary tektite. *Science* **257**, 954–958 (1992).
44. Pilkington, M., Hildebrand, A. & Ortiz-Aleman, C. Gravity and magnetic field modeling and structure of the Chicxulub crater, Mexico. *J. Geophys. Res.* **99**, 13147–13162 (1994).
45. Sharpton, V. L. et al. Model of the Chicxulub impact basin. *Geol. Soc. Am. Spec. Pap.* **307**, 55–74 (1996).

46. Espindola, J. M., Mena, M., Fuente, J. O. & Campos-Enriquez, J. O. A model of the Chicxulub impact structure (Yucatán, Mexico) based on gravity and magnetic signatures. *Phys. Earth Planet. Int.* **92**, 271–278 (1995).
47. Urrutia-Fucugauchi, J., Marin, L. & Trejo-Garcia, A. UNAM scientific drilling program of the Chicxulub impact structure — evidence for a 300-kilometre crater diameter. *Geophys. Res. Lett.* **23**, 1565–1568 (1996).
48. Kring, D. A. The dimensions of the Chicxulub impact crater and impact melt sheet. *J. Geophys. Res.* **100**, 16979–16986 (2005).
49. Morgan, J. & Warner, M. The third dimension of a multi-ring impact basin. *Geology* **27**, 407–410 (1999).
50. Grieve, R., Reimold, U., Morgan, J. V., Riller, U. & Pilkington, M. Observations and interpretations at Vredefort, Sudbury and Chicxulub: towards a composite model of a terrestrial impact basin. *Meteorit. Planet. Sci.* **43**, 855–882 (2008).
51. Christeson, G. et al. Mantle topography beneath the Chicxulub impact crater. *Earth Planet. Sci. Lett.* **284**, 249–257 (2009).
52. Christenson, G. L., Morgan, J. V. & Gulick, S. P. S. Mapping the Chicxulub impact stratigraphy and peak ring using drilling and seismic data. *J. Geophys. Res. Planets* **126**, e2021JE006938 (2021).
53. Barton, P. J. et al. Seismic images of Chicxulub impact melt sheet and comparison with the Sudbury structure. *Geol. Soc. Am. Spec. Pap.* **465**, 103–114 (2010).
54. Vermeesch, P. M. & Morgan, J. V. Structural uplift beneath the Chicxulub impact crater. *J. Geophys. Res.* **113**, B07103 (2008).
55. Gulick, S. P. S. et al. The first day of the Cenozoic. *Proc. Natl Acad. Sci. USA* **113**, 19342–19351 (2019).
56. Whalen, M. T. et al. Winding down the Chicxulub impact: the transition between impact and normal marine sedimentation near ground zero. *Mar. Geol.* **430**, 106368 (2020).
57. Ormö, J. et al. Assessing event magnitude and target water depth for marine-target impacts: ocean resurge deposits in the Chicxulub M0077A drill core compared. *Earth Planet. Sci. Lett.* **564**, 116915 (2021).
58. Kaskes, P. et al. Formation of the crater suevite sequence from the Chicxulub peak ring: a petrographic, geochemical, and sedimentological characterization. *GSA Bull.* **134**, 895–927 (2021).
59. Morgan, J. V. et al. Full-waveform tomographic images of the peak ring at the Chicxulub impact crater. *J. Geophys. Res.* **116**, B06303 (2011).
60. Christeson, G. L. et al. Extraordinary rocks from the peak ring of the Chicxulub impact crater: P-wave velocity, density, and porosity measurements from IODP/ICDP Expedition 364. *Earth Planet. Sci. Lett.* **495**, 1–11 (2018).
61. Gulick, S. P. S. et al. Geophysical characterization of the Chicxulub impact crater. *Rev. Geophys.* **51**, 31–52 (2013).
62. Elbeshausen, D., Wünnemann, K. & Collins, G. S. Scaling of oblique impacts in frictional targets: implications for crater size and formation mechanisms. *Icarus* **204**, 716–731 (2009).
63. Artemieva, N. & Morgan, J. Modeling the formation of the K–Pg boundary layer. *Icarus* **201**, 768–780 (2009).
64. Artemieva, N. et al. Quantifying the release of climate-active gases by large meteorite impacts with a case study of Chicxulub. *Geophys. Res. Lett.* **44**, 10180–10188 (2017).
65. Schultz, P. H. Effect of impact angle on vaporization. *J. Geophys. Res.* **100**, 21117–21135 (1996).
66. Pierazzo, E. & Melosh, H. J. Understanding oblique impacts from experiments, observations, and modeling. *Ann. Rev. Earth Planet. Sci.* **98**, 10–96 (2000).
67. Collins, G. S. et al. Dynamic modeling suggests asymmetries in the Chicxulub crater are caused by target heterogeneity. *Earth Planet. Sci. Lett.* **270**, 221–230 (2008).
68. Baker, D. M. et al. The formation of peak-ring basins: working hypothesis and path forward to constrain models of impact-basin formation. *Icarus* **273**, 146–163 (2016).
69. Rae, A. S. P. et al. Stress–strain evolution during peak-ring formation: a case study of the Chicxulub impact structure. *J. Geophys. Res. Planets* **124**, 396–417 (2019).
70. Ivanov, B. A. Numerical modelling of the largest terrestrial meteorite craters. *Sol. Syst. Res.* **39**, 381–409 (2005).
71. Head, J. W. Transition from complex craters to multi-ringed basins on terrestrial planetary bodies: scale-dependent role of the expanding melt cavity and progressive interaction with the displaced zone. *Geophys. Res. Lett.* **37**, L02203 (2010).
72. Rae, A. S. P. et al. Impact-induced porosity and micro-fracturing at the Chicxulub impact structure. *J. Geophys. Res.* **124**, 1960–1978 (2019).
73. Melosh, H. J. Acoustic fluidization: a new geologic process? *J. Geophys. Res. Solid. Earth* **84**, 7513 (1979).
74. Schultz, P. H. & D'Hondt, S. Cretaceous–Tertiary (Chicxulub) impact angle and its consequences. *Geology* **24**, 963–967 (1996).
75. Hildebrand, A. R. et al. Mapping Chicxulub crater structure with overlapping gravity and seismic surveys. In *29th Lunar and Planetary Science Conference* Abstract 1821 (Lunar and Planetary Institute, 1998).
76. Gault, D. E. & Wedekind, J. Experimental studies of oblique impact. In *Proc. 9th Lunar and Planetary Science Conference* 3843–3875 (Lunar and Planetary Institute, 1978).
77. Chapman, C. R. & McKinnnon, W. B. Cratering of planetary satellites. In *Satellites* 492–580 (Univ. Arizona Press, 1986).
78. Collins, G. S., Melosh, H. J. & Marcus, R. A. Earth Impact Effects Program: a web-based computer program for calculating the regional environmental consequences of a meteoroid impact on Earth. *Meteorit. Planet. Sci.* **40**, 817–840 (2005).
79. Koeberl, C. & Sigurdsson, H. Geochemistry of impact glasses from the K/T boundary in Haiti: relation to smectites, and a new type of glass. *Geochim. Cosmochim. Acta* **56**, 2113–2129 (1992).
80. Belza, J. S., Goderis, S., Montanari, A., Vanhaecke, F. & Claeys, P. Petrography and geochemistry of distal spherules from the K–Pg boundary in the Umbria–Marche region (Italy) and their origin as fractional condensates and melts in the Chicxulub impact plume. *Geochim. Cosmochim. Acta* **202**, 231–263 (2017).
81. Smit, J. The global stratigraphy of the Cretaceous–Tertiary boundary impact ejecta. *Ann. Rev. Earth Planet. Sci.* **27**, 75–113 (1999).
82. Goderis, S. et al. Globally distributed iridium layer preserved within the Chicxulub impact structure. *Sci. Adv.* **7**, eabe3647 (2020).
83. Kyte, F. T. & Smit, J. Regional variations in spinel compositions: an important key to the Cretaceous/Tertiary event. *Geology* **14**, 485–487 (1986).
84. Argyle, E. The global fallout signature of the K–T bolide impact. *Icarus* **77**, 220–222 (1989).
85. Melosh, H. J., Schneider, N. M., Zahnle, K. J. & Latham, D. Ignition of global wildfires at the Cretaceous/Tertiary boundary. *Nature* **343**, 251–254 (1990).
86. Alvarez, W., Claeys, P. & Kieffer, S. Emplacement of Cretaceous–Tertiary boundary shocked quartz from Chicxulub crater. *Science* **269**, 930–935 (1995).
87. Kring, D. A. & Durda, D. D. Trajectories and distribution of material ejected from the Chicxulub impact crater: implications for post-impact wildfires. *J. Geophys. Res.* **107**, 5062 (2002).
88. Johnson, B. C. & Melosh, H. J. Formation of spherules in impact produced vapor plumes. *Icarus* **217**, 416–430 (2012).
89. Pierazzo, E. & Melosh, H. J. Hydrocode modeling of oblique impacts: the fate of the projectile. *Met. Planet. Sci.* **35**, 117–130 (2000).
90. McGregor, P. J., Nicholson, P. D. & Allen, M. G. CASPIR observations of the collision of comet Shoemaker-Levy 9 with Jupiter. *Icarus* **121**, 361–388 (1996).
91. Colgate, S. A. & Petschek, A. G. *Cometary Impacts And Global Distributions Of Resulting Debris By Floating*. Report LA-UR-84-3911 (Los Alamos National Laboratory, 1985).
92. Goldin, T. J. *Atmospheric Interactions During Global Deposition Of Chicxulub Impact Ejecta*. PhD thesis, Univ. Arizona Tucson (2008).
93. Goldin, T. J. & Melosh, H. J. Self-shielding of thermal radiation by Chicxulub impact ejecta: firestorm or fizzle? *Geology* **37**, 1135–1138 (2009).
94. Lyons, S. L. et al. Organic matter from the Chicxulub crater exacerbated the K–Pg impact winter. *Proc. Natl Acad. Sci. USA* **117**, 25327–25334 (2020).
95. Pope, K. O., Baines, K. H., Ocampo, A. C. & Ivanov, B. A. Impact winter and the Cretaceous/Tertiary extinctions: results of a Chicxulub asteroid impact model. *Earth Planet. Sci. Lett.* **128**, 719–725 (1994).
96. Pope, K. O., Baines, K. H., Ocampo, A. C. & Ivanov, B. A. Energy, volatile production, and climatic effects of the Chicxulub Cretaceous/Tertiary impact. *J. Geophys. Res. Planets* **102**, 21645–21664 (1997).
97. Pierazzo, E., Hahmann, A. N. & Sloan, L. C. Chicxulub and climate: radiative perturbations of impact-produced S-bearing gases. *Astrobiology* **3**, 99–118 (2003).
98. Kring, D. A. The Chicxulub impact event and its environmental consequences at the Cretaceous–Tertiary boundary. *Palaeogeogr. Palaeoclimatol. Palaeoecol.* **255**, 4–21 (2007).
99. Kaiho, K. et al. Global climate change driven by soot at the K–Pg boundary as the cause of the mass extinction. *Sci. Rep.* **6**, 28427 (2016).
100. Robertson, D. S., Lewis, W. M., Sheehan, P. M. & Toon, O. B. K/Pg extinction: re-evaluation of the heat/fire hypothesis. *J. Geophys. Res. Biogeosci.* **118**, 329–336 (2013).
101. Morgan, J. V., Artemieva, N. & Goldin, T. Revisiting wildfires at the K–Pg boundary. *J. Geophys. Res. Biogeosci.* **118**, 1508–1520 (2013).
102. Belcher, C. M. et al. An experimental assessment of the ignition of forest fuels by the thermal pulse generated by the Cretaceous–Palaeogene impact at Chicxulub. *J. Geol. Soc.* **172**, 175–185 (2015).
103. Wolbach, W. S., Gilmour, I., Anders, E., Orth, C. J. & Brook, R. R. Global fire at the Cretaceous–Tertiary boundary. *Nature* **334**, 665–669 (1988).
104. Wolbach, W. S., Gilmour, I. & Anders, E. Major wildfires at the Cretaceous/Tertiary boundary. *Geol. Soc. Am. Spec. Pap.* **356**, 391–400 (1990).
105. Svetsov, V. & Shuvalov, V. Thermal radiation from impact plumes. *Meteorit. Planet. Sci.* **54**, 126–141 (2018).
106. Toon, O. B. et al. Evolution of an impact-generated dust cloud and its effects on the atmosphere. *Geol. Soc. Am. Spec. Pap.* **190**, 187–199 (1982).
107. Pope, K. O. Impact dust not the cause of the Cretaceous–Tertiary mass extinction. *Geology* **30**, 99–102 (2002).
108. Covey, C., Thompson, S. L., Weissman, P. R. & MacCracken, M. C. Global climatic effects of atmospheric dust from an asteroid or comet impact on Earth. *Glob. Planet. Change* **9**, 263–273 (1994).
109. Toon, O. B., Bardeen, C. & Garcia, R. Designing global climate and atmospheric chemistry simulations for 1 and 10km diameter asteroid impacts using the properties of ejecta from the K–Pg impact. *Atmos. Chem. Phys.* **16**, 13185–13212 (2016).
110. Howitz, A. et al. Revision and recalibration of existing shock classifications for quartzose rocks using low-shock pressure (2.5–20 GPa) recovery experiments and mesoscale numerical modeling. *Met. Planet. Sci.* **51**, 1741–1761 (2016).
111. Wdowiak, T. J. et al. Presence of an iron-rich nanophase material in the upper layer of the Cretaceous–Tertiary boundary clay. *Meteorit. Planet. Sci.* **36**, 123–133 (2010).
112. López-Ramos, E. Geological summary of the Yucatán Peninsula. In *Ocean Basins and Margins, the Gulf of Mexico and Caribbean* (eds Nairn, A. E. M. & Stehli, F. G.) 257–282 (Plenum Press, 1975).
113. Chiarenza, A. et al. Asteroid impact, not volcanism, caused the end-Cretaceous dinosaur extinction. *Proc. Natl Acad. Sci. USA* **117**, 17084–17093 (2020).
114. Ohno, S. et al. Production of sulphate-rich vapour during the Chicxulub impact and implications for ocean acidification. *Nat. Geosci.* **7**, 279–282 (2014).
115. Tang, W. et al. Widespread phytoplankton blooms triggered by 2019–2020 Australian wildfires. *Nature* **597**, 370–375 (2021).
116. Tyrrell, T., Merico, A. & Mckay, D. I. A. Severity of ocean acidification following the end Cretaceous asteroid impact. *Proc. Natl Acad. Sci. USA* **112**, 6556–6561 (2015).
117. Vellekoop, J. et al. Rapid short-term cooling following the Chicxulub impact at the Cretaceous–Paleogene boundary. *Proc. Natl Acad. Sci. USA* **111**, 7537–7541 (2014).
118. Vellekoop, J. et al. Shelf hypoxia in response to global warming after the Cretaceous–Paleogene boundary impact. *Geology* **46**, 683–686 (2018).
119. Milligan, J. N. et al. No evidence for a large atmospheric CO_2 spike across the Cretaceous–Paleogene boundary. *Geophys. Res. Lett.* **46**, 3462–3472 (2019).
120. Lomax, B., Beerling, D., Upchurch, G. & Otto-Bliesner, B. Rapid (10-yr) recovery of terrestrial productivity in a simulation study of the terminal Cretaceous impact even. *Earth Planet. Sci. Lett.* **192**, 137–144 (2001).

121. Vellekoop, J. et al. Evidence for Cretaceous–Paleogene boundary bolide impact winter conditions from New Jersey, USA. *Geology* **44**, 619–622 (2016).
122. Henehan, M. J. et al. Rapid ocean acidification and protracted Earth system recovery followed the end-Cretaceous Chicxulub impact. *Proc. Natl Acad. Sci. USA* **116**, 22500–22504 (2019).
123. Pierazzo, E. et al. Ozone perturbation from medium-size asteroid impacts in the ocean. *Earth Planet. Sci. Lett.* **299**, 263–272 (2010).
124. Thierstein, H. R. Terminal Cretaceous plankton extinctions: a critical assessment. *Geol. Soc. Am. Spec. Pap.* **190**, 358–399 (1982).
125. Sheehan, P. M. & Fastovksy, D. E. Major extinctions of land-dwelling vertebrates at the Cretaceous–Tertiary boundary, eastern Montana. *Geology* **20**, 556–560 (1992).
126. D'Hondt, S. Consequences of the Cretaceous/Paleogene mass extinction for marine ecosystems. *Annu. Rev. Ecol. Evol. Syst.* **36**, 295–317 (2005).
127. Thomas, E. in *Large Ecosystem Perturbations: Causes and Consequences* Vol. 424 (eds Monechi, S. et al.) https://doi.org/10.1130/2007.2424(01) (Geological Society of America, 2007).
128. Sessa, J. A., Bralower, T. J., Patzkowsky, M. E., Handley, J. C. & Ivany, L. C. Environmental and biological controls on the diversity and ecology of Late Cretaceous through early Paleogene marine ecosystems in the U.S. Gulf Coastal Plain. *Paleobiology* **38**, 218–239 (2012).
129. Sheehan, P. M. & Hansen, T. A. Detritus feeding as a buffer to extinction at the end of the Cretaceous. *Geology* **14**, 868–870 (1986).
130. Robertson, D. S., McKenna, M. C., Toon, O. B., Hope, S. & Lillegraven, J. A. Survival in the first hours of the Cenozoic. *Geol. Soc. Am. Bull.* **116**, 760–768 (2004).
131. D'Hondt, S., Donaghay, P., Zachos, J. C., Luttenberg, D. & Lindinger, M. Organic carbon fluxes and ecological recovery from the Cretaceous–Tertiary mass extinction. *Science* **282**, 276–279 (1998).
132. Coxall, H. K., D'Hondt, S. & Zachos, J. C. Pelagic evolution and environmental recovery after the Cretaceous–Paleogene mass extinction. *Geology* **34**, 297–300 (2006).
133. Kiessling, W. & Baron-Szabo, R. Extinction and recovery patterns of scleractinian corals at the Cretaceous–Tertiary boundary. *Palaeogeogr. Palaeoclimatol. Palaeoecol.* **214**, 195–223 (2004).
134. Dishon, G. et al. Evolutionary traits that enable scleractinian corals to survive mass extinction events. *Sci. Rep.* **10**, 3903 (2020).
135. Erickson, D. J. & Dickson, S. M. Global trace-element biogeochemistry at the K/T boundary: oceanic and biotic response to a hypothetical meteorite impact. *Geology* **15**, 1014–1017 (1987).
136. Hollis, C., Rodgers, K. & Parker, R. Siliceous plankton bloom in the earliest Tertiary of Marlborough, New Zealand. *Geology* **23**, 835–838 (1995).
137. Brinkhuis, H., Bujak, J., Smit, J., Versteegh, G. & Visscher, H. Dinoflagellate-based sea surface temperature reconstructions across the Cretaceous–Tertiary boundary. *Palaeogeogr. Palaeoclimatol. Palaeoecol.* **141**, 67–83 (1998).
138. Wendler, J. & Willems, H. Distribution pattern of calcareous dinoflagellate cysts across the Cretaceous–Tertiary boundary (Fish Clay, Stevns Klint, Denmark): implications for our understanding of species-selective extinction. *Geol. Soc. Am. Spec. Pap.* **356**, 265–276 (2002).
139. Sepúlveda, J. et al. Stable isotope constraints on marine productivity across the Cretaceous-Paleogene mass extinction. *Paleoceanogr. Paleoclimatol.* **34**, 1195–1217 (2019).
140. Sibert, E. C., Hull, P. M. & Norris, R. D. Resilience of Pacific pelagic fish across the Cretaceous/Palaeogene mass extinction. *Nat. Geosci.* **7**, 667–670 (2014).
141. Carvalho, M. R. et al. Extinction at the end-Cretaceous and the origin of modern Neotropical rainforests. *Science* **372**, 63–68 (2021).
142. Fastovsky, D. E. & Sheehan, P. M. The extinction of the dinosaurs in North America. *GSA Today* **15**, 4–10 (2005).
143. D'Hondt, S., Pilson, M. E., Sigurdsson, H., Hanson, A. K. & Carey, S. Surface-water acidification and extinction at the Cretaceous–Tertiary boundary. *Geology* **22**, 983–986 (1994).
144. Maruoka, T. & Koeberl, C. Acid-neutralizing scenario after the K–T impact event. *Geology* **31**, 489–492 (2003).
145. Gulick, S. et al. Site M0077: Upper peak ring. In *Proceedings of the International Ocean Discovery Program* Vol. 364 (IODP, 2017).
146. Gulick, S., et al. Site M0077: post impact sedimentary rocks. In *Proceedings of the International Ocean Discovery Program* Vol. 364 (IODP, 2017).
147. Rodríguez-Tovar, F. J., Lowery, C. M., Bralower, T. J., Gulick, S. P. & Jones, H. L. Rapid macrobenthic diversification and stabilization after the end-Cretaceous mass extinction event. *Geology* **48**, 1048–1052 (2020).
148. Berggren, W. A., Kent, D. V., Swisher III, C. C. & Aubry, M. P. *A Revised Cenozoic Geochronology And Chronostratigraphy* (SEPM, 1995).
149. Hull, P. M. & Norris, R. D. Diverse patterns of ocean export productivity change across the Cretaceous–Paleogene boundary: new insights from biogenic barium. *Paleoceanography* **26**, PA3205 (2011).
150. Lowery, C. M. et al. Early Paleocene paleoceanography and export productivity in the Chicxulub crater. *Paleoceanogr. Paleoclimatol.* **36**, e2021PA004241 (2021).
151. Seilacher, A., Reif, W.-E. & Westphal, F. Sedimentological, ecological and temporal patterns of fossil Lagerstätten. *Phil. Trans. R. Soc. Lond.* **31**, 5–23 (1985).
152. Briggs, D. E. G. Exceptionally preserved fossils. In *Palaeobiology 2* (eds Briggs, D. E. G. & Crowther, P. R.) 328–332 (Blackwell Publishing, 2001).
153. Bown, P. R. et al. A Paleogene calcareous microfossil Konservat-Lagerstätte from the Kilwa group of coastal Tanzania. *Geol. Soc. Am. Bull.* **120**, 3–12 (2008).
154. Kring, D. A. et al. Probing the hydrothermal system of the Chicxulub crater. *Sci. Adv.* **6**, eaaz3053 (2020).
155. Alegret, L., Thomas, E. & Lohmann, K. C. End-Cretaceous marine mass extinction not caused by productivity collapse. *Proc. Natl Acad. Sci. USA* **109**, 728–732 (2012).
156. Hull, P. M., Norris, R. D., Bralower, T. J. & Schueth, J. D. A role for chance in marine recovery from the end-Cretaceous extinction. *Nat. Geosci.* **4**, 856–860 (2011).
157. Alvarez, S. A. et al. Diversity decoupled from ecosystem function and resilience during mass extinction recovery. *Nature* **574**, 242–245 (2019).
158. Gibbs, S. J. et al. Algal plankton turn to hunting to survive and recover from end-Cretaceous impact darkness. *Sci. Adv.* **6**, eabc9123 (2020).
159. Sepúlveda, J., Wendler, J. E., Summons, R. E. & Hinrichs, K. U. Rapid resurgence of marine productivity after the Cretaceous-Paleogene mass extinction. *Science* **326**, 129–132 (2009).
160. Zachos, J. C., Arthur, M. A. & Dean, W. E. Geochemical evidence for suppression of pelagic marine productivity at the Cretaceous/Tertiary boundary. *Nature* **337**, 61–64 (1989).
161. Bown, P. R., Lees, J. A. & Young, J. R. Calcareous nannoplankton evolution and diversity through time. In *Coccolithophore* 481–508 (Springer, 2004).
162. Lyson, T. R. et al. Exceptional continental record of biotic recovery after the Cretaceous–Paleogene mass extinction. *Science* **366**, 977–983 (2019).
163. Cockell, C. S. et al. Shaping of the present-day deep biosphere at Chicxulub by the impact catastrophe that ended the Cretaceous. *Front. Microbiol.* **12**, 1413 (2021).
164. Bralower, T. J. et al. Origin of a global carbonate layer deposited in the aftermath of the Cretaceous–Paleogene boundary impact. *Earth Planet. Sci. Lett.* **548**, 116476 (2020).
165. Schenk, P. et al. Compositional control on impact crater formation on mid-sized planetary bodies: dawn at Ceres and Vesta, Cassini at Saturn. *Icarus* **359**, 114343 (2021).
166. Bray, V. J., Collins, G. S., Morgan, J. V., Melosh, H. J. & Schenk, P. M. Hydrocode simulation of Ganymede and Europa cratering trends — how thick is Europa's crust? *Icarus* **231**, 394–406 (2014).
167. Kyte, F. T. & Bostwick, J. A. Magnesioferrite spinel in Cretaceous–Tertiary boundary sediments of the Pacific basin: hot, early condensates of the Chicxulub impact. *Earth Planet. Sci. Lett.* **132**, 113–127 (1995).
168. Ebel, D. S. & Grossman, L. Spinel-bearing spherules condensed from the Chicxulub impact-vapor plume. *Geology* **33**, 293–296 (2005).
169. DePalma, R. A. et al. A seismically induced onshore surge deposit at the K–Pg boundary, North Dakota. *Proc. Natl Acad. Sci. USA* **116**, 8190–8199 (2019).
170. Stillwell, J. D. Patterns of biodiversity and faunal rebound following the K–T boundary extinction event in Austral Palaeocene molluscan faunas. *Palaeogeogr. Palaeoclimatol. Palaeoecol.* **195**, 319–356 (2003).
171. Rebolledo–Vieyra, M., Urrutia–Fucugauchi, J. & López–Loera, H. Aeromagnetic anomalies and structural model of the Chicxulub multiring impact crater, Yucatan, Mexico. *Rev. Mex. Cienc. Geol.* **27**, 185–195 (2010).
172. Shuvalov, V. Atmospheric erosion induced by oblique impacts. *Meteorit. Planet. Sci.* **44**, 1095–1105 (2009).
173. Collins, G. S. et al. The impact-cratering process. *Elements* **8**, 25–30 (2012).
174. Pierazzo, E. & Artemieva, N. Local and global environmental effects of impacts on Earth. *Elements* **8**, 55–60 (2012).
175. Turtle, E. P. et al. Impact structures: what does crater diameter mean? *Geol. Soc. Am. Spec. Pap.* **384**, 1–24 (2005).
176. Melosh, H. J. & Ivanov, B. A. Impact crater collapse. *Annu. Rev. Earth Planet. Sci.* **27**, 385–415 (1999).
177. O'Keefe, J. D. & Ahrens, T. J. Planetary cratering mechanics. *J. Geophys. Res.* **98**, 17011–17028 (1993).
178. Wünnemann, K. & Ivanov, B. A. Numerical modeling of the impact crater depth-diameter dependence in an acoustically fluidized target. *Planet. Space Sci.* **51**, 831–845 (2003).
179. Senft, L. & Stewart, S. T. Dynamic fault weakening and the formation of large impact craters. *Earth Planet. Sci. Lett.* **287**, 471–482 (2009).
180. Spray, J. G. & Thompson, L. M. Friction melt distribution in a multi-ring impact basin. *Nature* **373**, 130–132 (1996).

Acknowledgements

The authors thank S. Gulick and the rest of the Expedition 364 scientists for their invaluable contributions and thoughtful discussions. Expedition 364 was jointly funded by the European Consortium for Ocean Research Drilling (ECORD) and ICDP, with contributions and logistical support from the Yucatán State Government and Universidad Nacional Autónoma de México (UNAM). J.V.M. was funded by NERC grant NE/P005217/1. T.J.B. was funded by NSF-OCE 1736951. J.B. was funded through the VeWA consortium ("Past Warm Periods as Natural Analogues of our High-CO_2 Climate Future") by the LOEWE programme of the Hessen Ministry of Higher Education, Research and the Arts, Germany.

Author contributions

All authors contributed equally to the writing of this manuscript.

Competing interests

The authors declare no competing interests.

Peer review information

Nature Reviews Earth & Environment thanks O. Toon, C. Koeberl, and the other, anonymous, reviewer(s) for their contribution to the peer review of this work.

Publisher's note

Springer Nature remains neutral with regard to jurisdictional claims in published maps and institutional affiliations.